

# Tailoring Dynamical Codes for Biased Noise: The $X^3Z^3$ Floquet Code

F. Setiawan<sup>1,\*</sup> and Campbell McLauchlan<sup>2,3,†</sup>

<sup>1</sup>*Riverlane Research Inc., Cambridge, Massachusetts 02142, USA*

<sup>2</sup>*Centre for Engineered Quantum Systems, School of Physics,  
The University of Sydney, Sydney, NSW 2006, Australia*

<sup>3</sup>*Riverlane, Cambridge, CB2 3BZ, UK*

(Dated: November 8, 2024)

We propose the  $X^3Z^3$  Floquet code, a type of dynamical code with improved performance under biased noise compared to other Floquet codes. The enhanced performance is attributed to a simplified decoding problem resulting from a persistent symmetry under infinitely biased noise, which surprisingly exists in a code without constant stabilisers. Even if such a symmetry is allowed, we prove that a general dynamical code with two-qubit parity measurements cannot admit one-dimensional decoding graphs, a key feature resulting in the high performance of bias-tailored stabiliser codes. Despite this limitation, we demonstrate through our comprehensive numerical simulations that the symmetry of the  $X^3Z^3$  Floquet code renders its performance under biased noise far better than several leading Floquet code candidates. Furthermore, to maintain high-performance implementation in hardware without native two-qubit parity measurements, we introduce ancilla-assisted bias-preserving parity measurement circuits. Our work establishes the  $X^3Z^3$  code as a prime quantum error-correcting code candidate, particularly for devices with reduced connectivity, such as the honeycomb and heavy-hexagonal architectures.

## I. INTRODUCTION

Quantum error correction (QEC) [1–4] should be understood as occurring both in space and time [5]. Taking advantage of the temporal dimension, Floquet codes [6–15], or more generally dynamical codes [16, 17], form a large class of error-correcting codes, which can achieve competitive fault-tolerant performance while reducing the weights of check measurements performed during error-correction [6, 7, 9, 18]. Several of these codes [8–11] also benefit from being defined on a lattice with sparser connectivity than that for the surface code [19, 20]: each qubit is only connected to three other qubits. In architectures where two-qubit parity check measurements are native, Floquet codes could achieve higher thresholds [7, 21] than the surface code. Without requiring additional connectivity, this code can be deformed around defective components due to highly noisy qubits or gates [18, 22]. Moreover, dynamical codes allow for implementations of arbitrary Clifford, and even some non-Clifford gates, through low-weight parity check measurements [16].

Although Floquet codes (in particular, the honeycomb code) have been studied under various noise models [9, 23], there have not been any Floquet codes that are specifically tailored for an improved performance under biased noise. A biased noise model is one in which a specific type of error, for example, phase errors, occurs more frequently than other errors, such as bit flip errors. This biased noise is typical to most quantum platforms, for example, superconducting fluxonium qubits [24], bosonic “cat” qubits [25, 26], neutral atoms [27], quantum-dot spin qubits [28, 29] and Majorana qubits [30].

For enhanced performance, quantum-error-correcting codes need to be designed such that they possess symmetries that can be utilised to simplify the error-syndrome decoding problem given the noise structure [31–39]. While there have been several proposals on bias-tailored static codes [32–43], designing Floquet codes for high performance under biased noise is still an open problem. Owing to the experimental relevance of biased noise and given the ease of implementation of Floquet codes which require only two-qubit parity measurements, it is therefore imperative to tailor Floquet codes for biased noise and study how the performance of such dynamical codes can be improved.

In this paper, we present the  $X^3Z^3$  bias-tailored Floquet code, a Clifford-deformed [36] version of the Calderbank–Shor–Steane (CSS) Floquet code [10, 11]. Despite not having a fixed stabiliser group (as static codes have), the  $X^3Z^3$  Floquet code still possesses a symmetry under infinitely biased noise that allows for a simplified decoding in biased noise regimes. We perform an in-depth study of this code, along with the CSS Floquet code [10, 11], and two types of honeycomb codes: one proposed by Hastings and Haah [6] and the other by Gidney *et al.* [7]. We simulate all codes under biased-noise models, and find that the  $X^3Z^3$  code has the best performance. Using a matching decoder, we find that, as the noise changes from fully depolarising to pure dephasing, the  $X^3Z^3$  Floquet code threshold increases from 1.13% to 3.09% under a code-capacity noise model and increases from 0.76% to 1.07% under a circuit-level noise model mimicking hardware with noisy direct entangling measurements. Furthermore, we show that its sub-threshold performance is also substantially better under biased noise than other Floquet codes.

Compared to its static counterparts, the  $X^3Z^3$  Floquet code has an advantage that it can be realised using only

\* setiawan.wenming@riverlane.com

† campbell.mclauchlan@sydney.edu.au

two-qubit parity check measurements. This makes it particularly suitable for devices with constrained connectivity, such as the honeycomb and heavy-hexagonal lattice (currently IBM’s preferred superconducting-qubit architecture) [44, 45]. Moreover, we demonstrate that the two-qubit parity measurements of the Floquet code can be performed in a bias-preserving way even in hardware without direct entangling measurements, thus enabling high performance implementation in such devices.

To explain the performance of our bias-tailored Floquet code, we argue that other dynamical codes defined on the same architecture, and built from two-body measurements, would likely not have drastically improved performance compared to the  $X^3Z^3$  Floquet code. To support this argument, we prove that decoding graphs of such dynamical codes under infinitely biased noise have connectivities that are too high for the decoding problem to be reduced to a simple decoding of repetition codes, as is the case for static codes [35, 36]. This can be understood as resulting from the fact that error syndromes of dynamical codes possess less symmetry than their static code counterparts.

The paper is laid out as follows. In Sec. II, we review the basics of Floquet codes together with two commonly studied examples: honeycomb and CSS Floquet codes. Readers who are already familiar with Floquet codes can skip directly to Sec. III where we discuss our  $X^3Z^3$  Floquet code which is obtained by bias-tailoring the CSS Floquet code. Crucially, we show that there exists a persistent symmetry in the code’s error syndrome under the pure dephasing noise model that allows for simplified decoding. Subsequently, we introduce ancilla-assisted bias-preserving parity measurement circuits that allow for high-performance in devices without native entangling measurements. In Sec. IV, we present our simulation methods and noise models. We then provide our simulation results for all of the four Floquet codes studied in Sec. V. To explain the code performance, in Sec. VI we prove that a class of dynamical codes on the honeycomb lattice has high-connectivity decoding graphs. We also prove that dynamical codes with only two-qubit parity check measurements cannot have repetition-code-like decoding graphs, as is the case with static codes. Finally, we conclude and present future research directions in Sec. VII. In the Appendices, we give a more detailed review of the basics of honeycomb and CSS Floquet codes, and present the details of our noise models, numerical simulations, and theorems.

## II. BACKGROUND

### A. Dynamical and Floquet codes

We begin by defining dynamical and Floquet codes. In this paper, we consider the Floquet codes to be defined on the lattice of a two-dimensional colour code, which is trivalent and three-colourable. A trivalent lat-

tice has each vertex incident to three edges, and a three-colourable lattice has every face assigned one of three colours in such a way that there are no two adjacent faces of the same colour. Throughout this paper, we will use the honeycomb lattice as an example of such a lattice (see Fig. 1).

We define qubits as residing on the vertices of the lattice and error-correction will be performed by measuring two-qubit operators defined on edges of the lattice (i.e., acting on qubits incident to a given edge). Edges may be assigned a colour: each edge is coloured the same as the plaquettes it connects. We perform error-correction by measuring edge operators in a particular sequence. After any given round of edge measurements, the system will be in the  $+1$ -eigenstate of the operators in an “instantaneous stabiliser group” (ISG), which will change at each time step. The ISG at time step  $t + 1$  is defined as:

$$\begin{aligned} \text{ISG}_{t+1} = \langle S, \pm M \mid M \in \mathcal{M}_t, S \in \text{ISG}_t, \\ \text{such that } [S, M] = 0, \forall M \in \mathcal{M}_t. \end{aligned} \quad (1)$$

In the above,  $\mathcal{M}_t$  is the set of “check” measurements performed at time step  $t$ . The  $\text{ISG}_{t+1}$  also includes “plaquette stabiliser operators”  $S \in \text{ISG}_t$  which commute with all  $M \in \mathcal{M}_t$ . The check measurement operators are chosen in such a way that those check operators at time  $t$  that have overlapping qubit supports with check operators at  $t + 1$  anti-commute. For Floquet codes, the measurement sequence is periodic, such that  $\mathcal{M}_{t+T} = \mathcal{M}_t$  for some integer  $T$ . For such a code, we will be performing quantum memory experiments with  $mT$  time steps, for some integer  $m$ . We will refer to  $m$  as the number of “QEC rounds” in the experiment, while we will refer to  $mT$  as the number of “measurement subrounds” in the experiment.

The logical operators at time  $t$  are given by  $\mathcal{C}(\text{ISG}_t)/\text{ISG}_t$ , where  $\mathcal{C}(\text{ISG}_t)$  is the centraliser of  $\text{ISG}_t$ , i.e., the group of Pauli operators commuting with all  $S \in \text{ISG}_t$ . A (potentially trivial) logical operator “representative” is some member of  $\mathcal{C}(\text{ISG}_t)$ . Each nontrivial logical operator representative for the codes considered will be a string-like Pauli operator at each time step (see Fig. 1). To avoid anti-commuting with the next-subround edge measurements, certain check measurement results along a logical operator’s path have to be multiplied into that logical operator. Hence, the logical operators will evolve from one time step to the next.

We can detect errors if we can find sets of measurements, called detectors, that always multiply to the value  $+1$  in the absence of noise, thus registering no error. Over some number of QEC rounds we will have extracted several detector outcomes. A detector (or decoding) hypergraph is formed by first defining a node for each (independent) detector in the code’s history. Subsequently, for each potential fault (e.g., Pauli or measurement errors) that might have occurred, a (hyper)edge is drawn between the detectors whose signs are flipped by this fault. Each (hyper)edge is assigned a weight based on the probability of the corresponding error occurring [46]. The codes

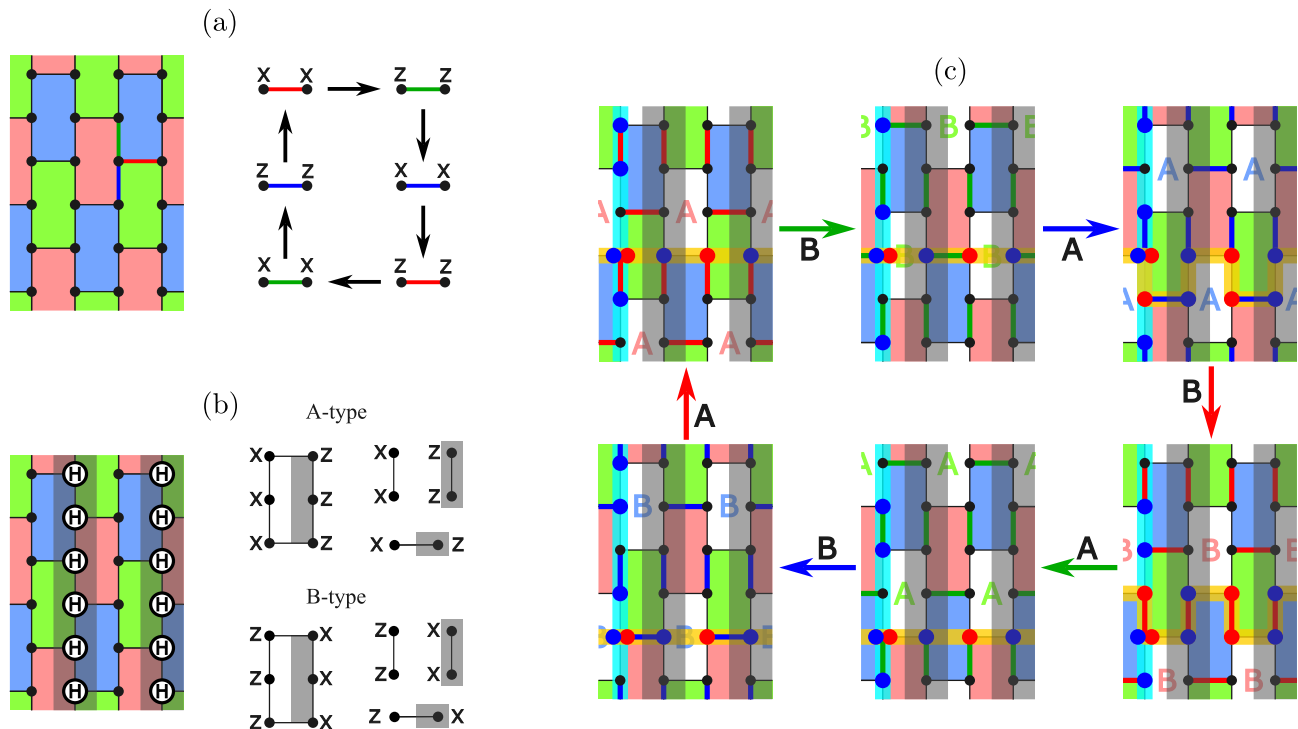


FIG. 1. (a) CSS and (b,c)  $X^3Z^3$  Floquet codes. (a,b) Left: Hexagonal lattice with qubits sitting on vertices and opposite boundaries identified. Plaquettes are assigned one of three colours (red, green, blue) and one of two types (X- or Z-type for CSS and A- or B-type for  $X^3Z^3$ ). (a) Right: CSS Floquet code measurement schedule. (b) The  $X^3Z^3$  Floquet code can be obtained from the CSS code via Hadamard gates applied to shaded domains shown (left). Right: Plaquette and edge (check) operators are A- or B-type, depending on their support on shaded/unshaded domains. (c) The  $X^3Z^3$  Floquet code measurement schedule. Arrows indicate the type and colour of the edge operator measured at each step, where the edges just measured (members of the ISG) are highlighted in the lattice. Uncoloured plaquettes host only a single type of stabiliser, either A or B, indicated by the letters in the plaquettes, while coloured plaquettes host both A- and B-type stabilisers for the ISG. One set of anti-commuting logical operators is shown by yellow and light blue strings, where their  $X$  ( $Z$ ) support on qubits is highlighted in red (blue). The other set (not shown) is similar to the set shown but offset by three measurement subrounds and with the  $X \leftrightarrow Z$  interchange of the qubit supports' bases.

we will be examining are amenable to minimum-weight perfect matching decoding [47], upon decomposing hyperedges into edges. Given a “syndrome” (a set of detectors whose measurements return  $-1$  rather than  $+1$ ), the decoder attempts to pair up the triggered detectors to determine a shortest-path correction operation. The decoder succeeds if the error combined with the correction is a trivial logical operator.

Having discussed the general idea of Floquet codes, we now briefly review the commonly studied examples of the code: two variants of the honeycomb code [6, 7], whose performance will also be investigated under biased noise, and the CSS Floquet code [10, 11]. We will later modify the CSS Floquet code to achieve the bias-tailored  $X^3Z^3$  Floquet code. More details of the honeycomb and CSS Floquet codes are presented in Appendix A.

## B. Honeycomb codes

We begin by first discussing the honeycomb codes. The first variant is due to Gidney *et al.* [7], which we call the  $P^6$  Floquet code, since its plaquette operators are six-body operators of the form  $P^{\otimes 6}$  for  $P = X, Y, Z$ . We define edge operators of three types: on red edges we define an  $XX$  operator, on green edges a  $YY$  operator and on blue edges a  $ZZ$  operator. We measure edge operators in the periodic sequence  $r \rightarrow g \rightarrow b$ . When this code is defined with periodic boundary conditions it stores two logical qubits (it is equivalent to the toric code concatenated with a two-qubit repetition code at each time step [6]). The code’s logical operators evolve through the measurement cycle (see Appendix A 1). While the measurement sequence has period 3, the logical operators only return to their initial values (up to signs) with period 6.

We define one stabiliser operator for each plaquette, such that blue plaquettes host  $Z^{\otimes 6}$  operators, red plaquettes host  $X^{\otimes 6}$  operators and green plaquettes host  $Y^{\otimes 6}$  operators. These plaquette operators are inferred

from edge measurements in two consecutive rounds. Detectors are formed from consecutive plaquette operator measurements.

The second honeycomb code variant, which we call the  $XYZ^2$  honeycomb code, is due to Hastings and Haah [6]. It differs from the  $P^6$  code by single-qubit Clifford rotations acting on the qubits. While edges are still coloured red, green or blue, edge operators have their Pauli bases defined according to their orientations within each T junction, i.e., horizontal edges are of  $Z$  type while the  $X$  and  $Y$  checks are respectively those edges which are  $90^\circ$  clockwise and counter-clockwise from the horizontal edges (see Appendix A 1). All plaquettes have the same stabiliser operator, i.e., the  $XYZ^2$  operator. While the logical operators of the  $XYZ^2$  code have the same qubit supports as those of the  $P^6$  code, the qubit support bases of the  $XYZ^2$  logical operators are not uniform throughout, but involve  $X$ ,  $Y$ , and  $Z$  Paulis [6]. We note that even though these honeycomb code variants have been studied by several works in the literature (e.g., Refs. [6–9]), there have not been any studies comparing the performance of these two codes under biased noise.

### C. CSS Floquet codes

Having discussed the honeycomb codes, we now give a brief review of another type of Floquet code, the CSS Floquet code which was proposed in Refs. [10, 11]. The CSS Floquet code is defined on the same honeycomb lattice. We show the code’s measurement cycle in Fig. 1(a). We measure operators defined on edges using the  $r \rightarrow g \rightarrow b$  cycle, but alternate between measuring  $XX$  and  $ZZ$  operators on these edges. Hence, this code has a period-6 measurement cycle, and its logical operator evolutions also have period-6. Even though a honeycomb code’s measurement schedule has only a period of 3, for consistency, we will define 1 QEC round to be 6 measurement subrounds for all codes studied in this paper. The check operators, stabilisers and logicals all are either  $X$ - or  $Z$ -type and, for this reason, the code is similar to static CSS codes.

Unlike the honeycomb codes, the CSS Floquet code has no persistent stabiliser operators. Instead, each ISG contains  $X$ -type and  $Z$ -type stabiliser operators defined on two of the three colours of plaquette and *either* an  $X$ -type *or* a  $Z$ -type operator defined on the other colour. For instance, after measuring red- $X$  checks, the ISG contains  $X^{\otimes 6}$  and  $Z^{\otimes 6}$  blue and green plaquette operators, but only  $X^{\otimes 6}$  red plaquette operators, since  $Z^{\otimes 6}$  red plaquette operators anti-commute with the red- $X$  checks. See Appendix A for more details.

Plaquette operators are measured in a single measurement subround, and detectors are formed from the consecutive measurements of these plaquette operators, whenever their results can be compared. Plaquette operators anti-commute with check measurements at certain measurement subrounds and hence, we cannot necessar-

ily form a detector at a plaquette every time a plaquette operator is measured (see Appendix A 2).

The CSS Floquet code is naturally suited to minimum-weight perfect matching (MWPM) decoding, since single-qubit ( $X$  or  $Z$ ) Pauli errors and measurement errors all lead to graph-like syndromes [11]: they each trigger a pair of detectors. There are two decoding graphs formed from the  $Z$ -type and  $X$ -type detectors. Only  $Y$  errors form hyperedges that need to be decomposed into edges in the two detector graphs.

### III. $X^3Z^3$ BIAS-TAILORED FLOQUET CODE

We now describe the  $X^3Z^3$  bias-tailored Floquet code, which is shown in Figs. 1(b) and 1(c). This code is related to the CSS Floquet code by Hadamard gates applied to the qubits in strips [shown in grey in Fig. 1(b)] along vertical non-trivial cycles of the lattice, and is a Floquetified version of the domain wall colour code [36]. We therefore still have two types of plaquettes and edges, one type originating from Pauli  $X$  plaquettes and edges before the Hadamard gates are applied, and the other originating from Pauli  $Z$  operators. We refer to these modified operators as A-type and B-type, respectively. They are defined in Fig. 1(b). The measurement sequence is analogous to the CSS Floquet code sequence:  $rA \rightarrow gB \rightarrow bA \rightarrow rB \rightarrow gA \rightarrow bB$ , where  $cA$  represents the measurement of A-type check operators along  $c$ -coloured edges, and similarly for  $cB$ . Just as with the CSS Floquet code [11], this code can also be defined on a planar lattice with boundary.

The decoding of the  $X^3Z^3$  Floquet code under  $Z$ -biased noise is simplified by the presence of a symmetry in the decoding graphs. This is a space-time analogue of the symmetries present in bias-tailored static codes such as the  $XZZX$  code [35] and the domain wall colour code [36]. In such codes, under the code-capacity noise model (with only single-qubit Pauli errors), syndromes resulting from Pauli errors of a single type, such as  $Z$  errors, are forced to come in pairs along one-dimensional strips of the lattice. This results from strips of stabilisers multiplying together to an operator that commutes with all  $Z$  errors: these are one-dimensional symmetries of the stabiliser code under infinitely biased noise. We will refer to stabilisers in an ISG that are flipped by an error as anyons. In bias-tailored static codes, anyons can propagate within strips but cannot move outside the strip without changing Pauli type. We will see that in the case of the bias-tailored Floquet code, there exists a similar symmetry.

As in the CSS Floquet code, there are two disjoint decoding graphs, the A-type and B-type graphs, whose edges correspond to single-qubit Pauli errors. In even measurement subrounds, we perform B-type measurements and form detectors for the B-type graph while in odd measurement subrounds we only form detectors for the A-type graph. Note that under a more complicated

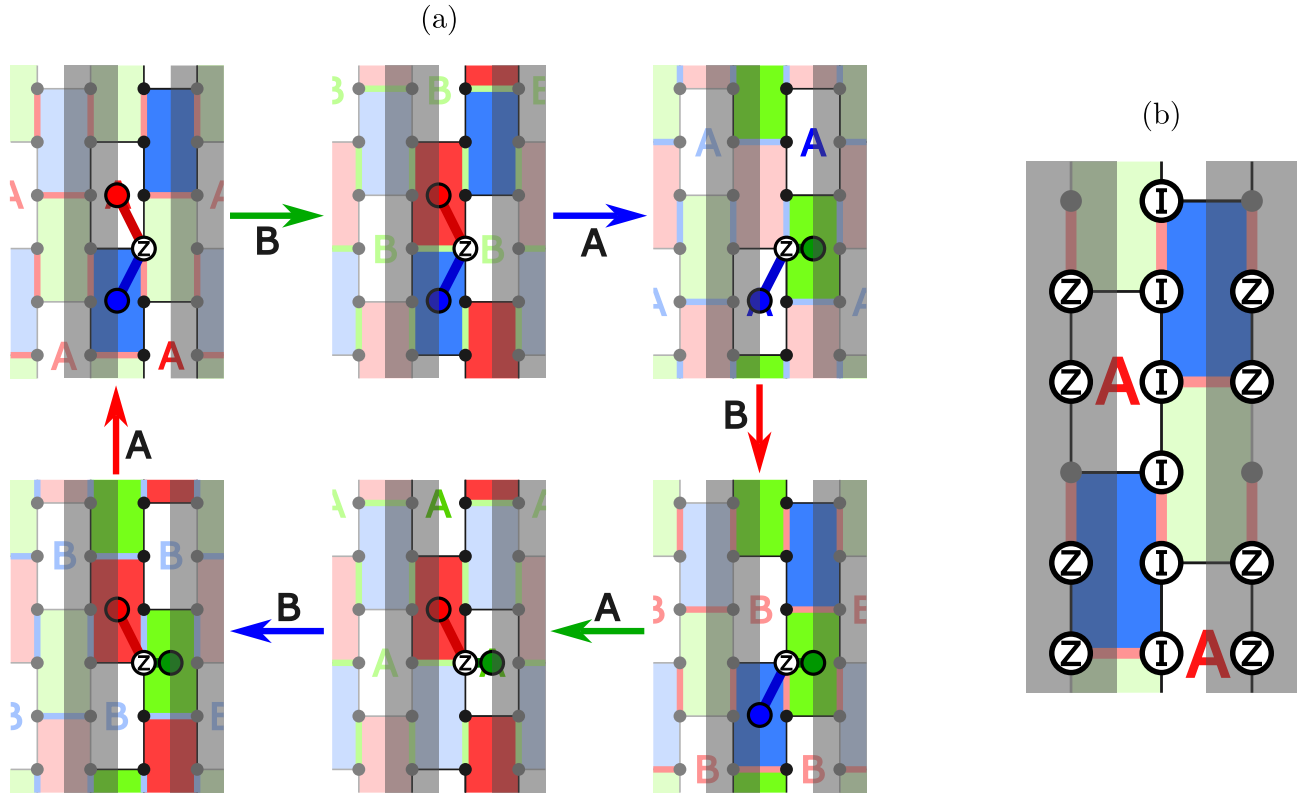


FIG. 2. Persistent symmetry of the  $X^3Z^3$  Floquet code leads to improved performance under  $Z$ -biased noise. (a) An example of such a symmetry, along with a Pauli- $Z$  error, is shown throughout the measurement cycle for the Floquet code. Arrows indicate the type of check measurements ( $cA$  or  $cB$  for some colour  $c$ ) performed in each subround. A-type plaquette operators that form part of the ISG at that subround are highlighted in darker colours. The product of these operators gives rise to a persistent symmetry under infinitely  $Z$ -biased noise. Anyons associated with a single Pauli- $Z$  error are shown at each subround: these always appear in pairs along the vertical strip in which the  $Z$  error is contained. (b) An example of a symmetry after  $rA$  checks are measured. Since the product of red and blue A-type plaquettes along this vertical strip commutes with the noise, the syndromes must appear in pairs along this vertical strip.

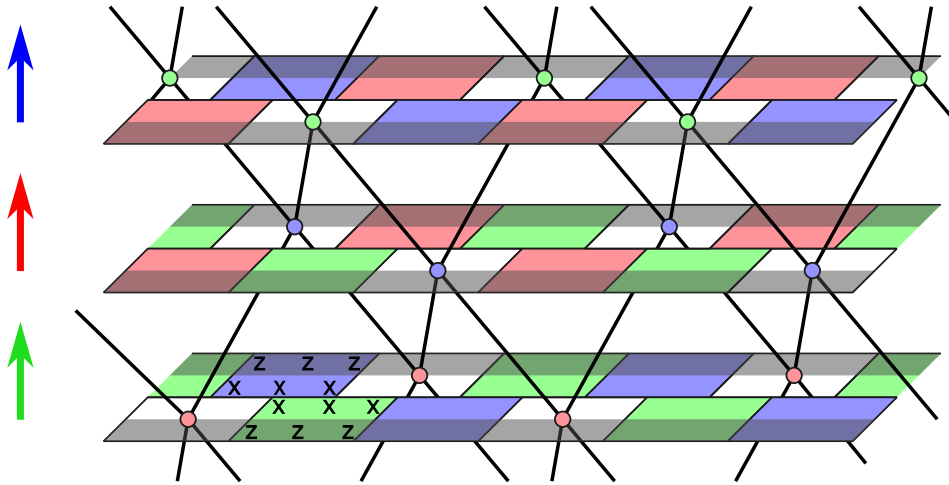


FIG. 3. The A-type detector graph of the  $X^3Z^3$  Floquet code under infinitely biased noise. Only a single vertical strip [e.g., that supporting the symmetry] is shown in Fig. 2(b). The illustrated part of the graph is disconnected from that of any neighbouring strip. The A-type measurement subrounds are shown with arrows on the left; the B-type subrounds are not shown, since they do not influence the detectors in this graph. Nodes (representing detectors) are placed at the position of the corresponding plaquette and at the subround in which it is measured to form a detector. For example, the bottom layer corresponds to blue A-check measurements, at which time red A-type plaquettes are measured.

noise model, such as one including measurement errors or two-qubit depolarising errors, edges can exist between the A- and B-type graphs and they are no longer disjoint.

### A. Persistent symmetry and two-dimensional decoding under biased noise

There is no constant stabiliser group when viewing the  $X^3Z^3$  Floquet code as a subsystem code (in a subsystem code, the stabiliser group is defined as the center of the gauge group) [10, 11]. Surprisingly, despite this fact, there do exist operators at every time step that form a symmetry under infinitely  $Z$ -biased noise (without measurement errors). These symmetry operators at time step  $t$ , are formed by plaquette operators of a single type along vertical strips of the lattice; symmetries on unshaded and shaded strips are formed by A- and B-type plaquettes, respectively (see Fig. 2). We take, as these symmetries, the product of all such plaquette operators that commute with all operators in  $\mathcal{M}_{t+1}$  (the set of check measurements to be performed in the next subround). To see why the symmetry is formed at each measurement subround, consider one particular time step as shown in Fig. 2(a), i.e., after red A-type measurements. As depicted, the product of red and blue A-type plaquettes is the identity on all qubits in the unshaded vertical strip, and acts as  $Z$  on some qubits in the shaded vertical strips. A similar symmetry can be formed by blue and green B-type plaquettes on shaded strips in this subround.

As a result of this symmetry, Pauli- $Z$  errors create anyons in pairs along vertical strips. An example of such anyons is shown in each measurement subround of Fig. 2(b). Note that the anyons change plaquette locations between subrounds, but always respect the symmetry. These anyons in Fig. 2 represent detectors that would be triggered if the Pauli- $Z$  error shown occurred at that time step. For example, if the  $Z$  error occurs immediately after the red A-check measurements, it will trigger a red detector after subsequent blue A-check measurements and a blue detector after green A-check measurements.

Unlike the symmetry in static stabiliser codes, this symmetry does not allow for one-dimensional decoding even without measurement errors. While in static codes, only measurement errors produce “time-like” edges, in Floquet codes, even Pauli errors produce time-like edges (between detectors formed at different times). To demonstrate this, we display in Fig. 3 a portion of the A-type detector graph under infinitely biased noise (with no measurement errors). As can be seen, there is a disconnected sub-graph defined along one vertical strip of the code lattice. Even considering only single-qubit Pauli noise without measurement errors, the decoding graph in the infinite bias regime is two-dimensional (i.e., the graph is planar). This results from the fact that neighbouring plaquettes are measured at different times. We emphasise

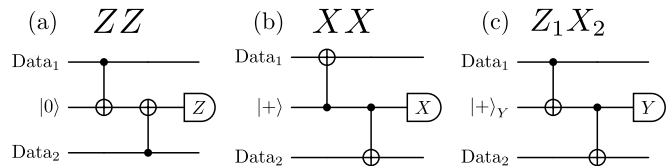


FIG. 4. Depth-2 check measurement circuits using CNOT gates along with resets and single-qubit measurements in the  $Z$ ,  $X$  and  $Y$  bases for (a)  $Z_1Z_2$ , (b)  $X_1X_2$ , and (c)  $Z_1X_2$  checks, respectively.

that although the above discussion is based on  $Z$  errors, the same analysis also holds for  $X$  errors because  $X$  and  $Z$  operators are interchangeable for the  $X^3Z^3$  code. As a result, the performance of the  $X^3Z^3$  code under  $X$ -biased noise is expected to be the same as that under the  $Z$ -biased noise model studied in this paper.

### B. Bias-preserving parity-check circuits

While two-body measurements are native to certain architectures, for example, Majorana qubits [21, 48], most architectures require a syndrome extraction circuit to carry out such measurements. To maintain the high-performance of bias-tailored codes in these hardwares, the syndrome extraction circuits need to be constructed in a bias-preserving manner, such that they propagate errors in such a way so as to sustain the noise bias. To this end, we design two-qubit parity check circuits that preserve the  $Z$  bias on data qubits. That is, the probability of  $X$  and  $Y$  errors on data qubits after these circuits is small (proportional to single-qubit  $X$  or  $Y$  error probabilities). A bias-preserving parity check measurement circuit can be constructed by using an ancilla circuit connecting two data qubits, which can be realised even in devices with minimal connectivity, such as the heavy-hexagonal layout. [44, 45].

For a circuit to be generally bias-preserving, it needs to be constructed using only gates that do not change the error type under conjugation. For example, to preserve the  $Z$ -bias,  $Z$  errors cannot be propagated to either  $X$  or  $Y$  errors on data qubits. One way to construct bias-preserving circuits is to use only CNOT gates in the measurement circuits as CNOT gates propagate errors to others with the same Pauli type. For the  $X^3Z^3$  code, we need to construct bias-preserving circuits for three different kinds of parity checks:  $XX$ ,  $ZZ$  and  $XZ$ . All these three circuits can be constructed using only CNOT gates as shown in Fig. 4. As depicted, these circuits also include resets and measurements of the ancilla qubit in the Pauli bases, i.e.,  $Z$ ,  $X$  and  $Y$  bases for  $ZZ$ ,  $XX$  and  $XZ$  checks, respectively. Note that the circuits are still bias-preserving even if the resets/measurements in the  $X$  and  $Y$  bases are compiled in terms of resets/measurements in the  $Z$  basis with additional single-qubit Clifford gates. This is because the  $Z$  error on any qubit at every time

step in the compiled circuits still propagates to data qubits as a  $Z$  error, or as a check operator about to be measured.

In realistic systems, errors can occur during the application of the gate. If conventional CNOT gates are used in the syndrome extraction circuits, then they may not preserve the noise bias. This is because a  $Z$  error occurring on the target qubit during the application of the CNOT gate results in a combination of  $Z$  and  $X$  errors on the target qubit after the CNOT gate [49].

One way to construct a circuit that preserves the noise bias in the presence of mid-gate errors is to use bias-preserving CNOT gates [49]. These bias preserving CNOT gates, however, are restricted to only specific platforms, such as the cat qubit platform. Here, we propose a general approach to constructing  $Z$ -bias preserving parity check circuits. While our proposed circuits can preserve only a specific type of noise bias, i.e., the  $Z$  bias, these circuits are built using conventional two-qubit gates and thus can be implemented in many different architectures. The idea is to use the CZ gates as these do not propagate  $Z$  errors, including the mid-gate  $Z$  errors, into other kinds of errors [49]. If this is not possible, we can apply CNOT gates with ancillas as target qubits. In the following, we use this idea to construct fully bias-preserving circuits for the three parity checks shown in Fig. 4.

The simplest of these circuits is the depth-2  $ZZ$  measurement circuit, shown in Fig. 5(a) which is built using CZ gates. This circuit is equivalent to the one shown in Fig. 4. On the other hand, to implement an  $XX$  measurement, we utilise a depth-4 circuit as shown in Fig. 5(b) which is constructed from CNOT gates which use ancillas as target qubits. Note that, in this circuit, the two single-qubit  $X$  measurements on the data qubits in the middle of the circuit will not reveal the information of each of data qubit's state since before the measurements, we entangle each of the data qubits to the ancilla qubit using a CNOT gate. The mid-circuit  $X$  measurements on  $\text{Data}_1$  and  $\text{Data}_2$  qubits are equivalent to  $X_1X_a$  and  $X_2X_a$  measurements, respectively, where  $X_a$  acts on the ancilla qubit in the  $|0\rangle$  state. The final  $Z_a$  measurement disentangles the ancilla qubit, leaving the data qubits in an eigenstate of  $X_1X_2$ . This circuit therefore performs the required  $XX$  check measurement.

Finally, the  $Z_1X_2$  checks can be measured by performing CZ gates directly between the data qubits, as shown in Fig. 5(c). However, without connections between the data qubits in hardware with a heavy-hexagonal lattice, these CZ gates have to be implemented using ancilla qubits in-between the data qubits. To this end, we prepare the ancilla in the  $|+\rangle$  state and use a depth-3 circuit to implement this CZ gate (see the right-hand side of Fig. 5(c)); this is adapted from a similar circuit in Ref. [44]). The end result is a depth-6 measurement circuit. In Fig. 5(c), we provide optional measurements, coloured in grey, which provide “flag information” for detecting  $Z$  errors on the measurement ancilla that may

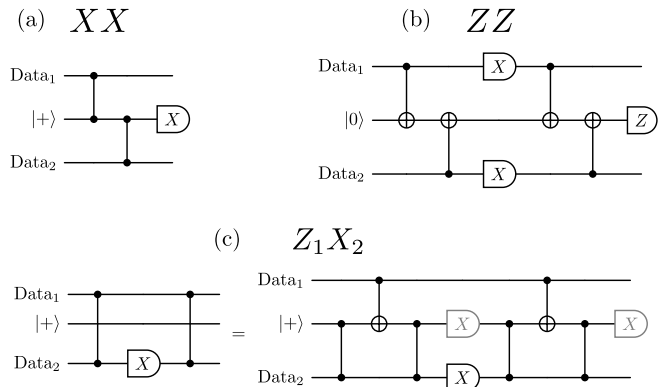


FIG. 5. Measurement circuits for (a)  $ZZ$ , (b)  $XX$ , and (c)  $Z_1X_2$  checks that preserve the  $Z$  noise bias on data qubits. Data qubits are labelled by  $\text{Data}_1$  and  $\text{Data}_2$ , while the middle qubit in each circuit is a measurement ancilla. In (c), the equality can be checked by noting that the depth-3 circuit before and after the measurement performs a next-nearest-neighbour CZ gate, if the measurement ancilla is initially in the  $|+\rangle$  state. The grey measurements can be optionally included to provide flag information.

have propagated to the data qubits.

We emphasise that, even if the  $X$  measurements in the parity-check circuits above are implemented using  $Z$  measurements sandwiched by Hadamard gates, the circuits are still bias preserving since a  $Z$  error occurring between those Hadamard gates is harmless. This is because a  $Z$  error happening before the measurement is immediately absorbed by the  $Z$  measurement without flipping its outcome, and a  $Z$  error after the measurement is a stabiliser of the state (up to a sign), so does nothing. Moreover, if the Hadamard gates are noisy, the single-qubit gate errors in many architectures are not the predominant error and are usually much smaller than those of the two-qubit gate errors [50–53].

#### IV. METHODS

We perform quantum memory experiment simulations of all codes mentioned above: the CSS and  $X^3Z^3$  Floquet codes together with the  $P^6$  and  $XYZ^2$  honeycomb codes, with varying degrees of noise bias  $\eta$ . The noise bias  $\eta = p_z/(p_x + p_y)$  is defined as the ratio of the  $Z$ -error  $p_z$  to other errors where the total physical error rate is  $p = p_x + p_y + p_z$ . As the noise asymmetry increases, the noise bias  $\eta$  increases from  $\eta = 0.5$  which corresponds to a fully depolarising noise ( $p_x = p_y = p_z = p/3$ ) to  $\eta = \infty$  corresponding to a pure  $Z$ -bias noise ( $p_z = p$ , and  $p_x = p_y = 0$ ).

We use two different biased noise models which are the generalisations of the standard code-capacity and standard depolarising entangling measurement (SDEM3) [9, 18] noise models to biased noise channels. The code-capacity noise model is one in which only single-qubit er-

rors are applied to all data qubits at every measurement subround. We note that, since for Floquet codes one QEC round consists of several measurement subrounds, the single-qubit noise channel in the code-capacity model is applied several times in one QEC round instead of just once as is the case with static codes. The code-capacity noise model is often used as a preferred initial noise model to study before going to a more involved model as its simplicity often offers insight into understanding the code performance. On the other hand, the SDEM3 model is a more elaborate error model involving single-qubit noise channels after every single-qubit gate, measurement and reset, a two-qubit noise channel after every multi-Pauli product (MPP) parity measurement gate, and a classical flip after each measurement. As in Ref. [9], we assume that each of these error channels occurs with a total probability  $p$ . The SDEM3 noise model is therefore close to standard circuit-level noise and would be a more accurate description of a realistic noise channel, particularly in hardware with native two-qubit measurements, for example, Majorana qubits [21, 48]. To take into account biased noise for the MPP gates, we here generalise the SDEM3 noise model in Refs. [9, 18]. The details of the biased code-capacity and SDEM3 noise models can be found in Appendix B.

We simulate the circuits and generate the error syndromes using Stim [54]. To decode the error syndromes, we apply a minimum-weight perfect matching (MWPM) decoder, which is implemented using PyMatching [47]. Our simulations are run for codes with effective distances  $d_{\text{eff}} \equiv d/2 = 4, 6, 8, 10, 12$ , where the effective distance  $d_{\text{eff}}$  is defined as the minimum number of faults under SDEM3 depolarising noise that produce a logical error, which is half of the distance  $d$  of the code-capacity noise model. The calculated effective distance differs between noise models since in the SDEM3 noise model, two-qubit errors occurring after an MPP parity gate count as a single fault, while under the code-capacity noise model they would count as two faults. We choose lattices of size  $2d_{\text{eff}} \times 3d_{\text{eff}}$  for the distances mentioned, and with periodic boundary conditions. We simulate the memory experiments for  $3d_{\text{eff}}$  QEC rounds, with each round containing 6 subrounds of check measurements.

## V. RESULTS AND DISCUSSION

The upper panels of Fig. 6 show the thresholds of all codes for various levels of noise bias  $\eta$  calculated for (a) code-capacity and (b) SDEM3 noise models. Each threshold is obtained from the intersection of the logical failure probabilities  $p_L$  vs physical error rate  $p$  curves of different code distances  $d_{\text{eff}} = d/2 = 6, 8, 10$  and 12. The data of  $p_L$  as a function of  $p$  for each code and various noise-bias strengths, used to obtain the thresholds, are presented in Figs. 11-14 of Appendix C.

Since the code-capacity noise model which considers only single-qubit noise is a more benign model than

the SDEM3 noise model which also includes two-qubit and measurement errors, the code performance calculated under the code-capacity noise is better than that of the SDEM3 noise. For both noise models, as shown in Figs. 6(a) and 6(b), the performance of the  $X^3Z^3$  code becomes increasingly better than those of all other tested codes as the noise bias increases. In particular, as the noise changes from fully depolarising to a pure dephasing type, the  $X^3Z^3$  Floquet code's threshold increases from  $\approx 1.13\%$  to  $\approx 3.09\%$  for the code-capacity noise and from  $\approx 0.76\%$  to  $\approx 1.08\%$  for the SDEM3 noise model. The threshold therefore increases by a factor of 2.7 and a factor of 1.4 for the code capacity and SDEM3 noise models, respectively. We also investigate the performance of the  $X^3Z^3$  Floquet code with a twisted periodic boundary condition where we find that the threshold at the infinite bias can reach up to  $\approx 4.4\%$  (see Appendix F). This increased in the threshold of the twisted code is due to the fact that the pure  $Z$ -type logical operators has a length that scales quadratically with the distance of the untwisted code, thereby increases its code distance. We note, however, that the advantage of the twisted over the untwisted code only holds for the noise regime which is close to the infinite bias. As shown in Figs. 6(a) and 6(b), while the CSS Floquet code has the same threshold as the  $X^3Z^3$  code when the noise is fully depolarising, its threshold decreases with increasing noise bias. This decrease is due to the fact that the CSS Floquet code has pure  $X$  and pure  $Z$  detectors: in the presence of biased noise, half of the detectors which are of the same type of the dominant error will become less useful in detecting the biased errors.

Figures. 6(a) and 6(b) show that the thresholds for the honeycomb codes have only minor improvements as the noise bias increases. For the fully depolarising code-capacity noise, all codes have the same threshold, whereas for the SDEM3 depolarising noise the honeycomb code thresholds are about 1.3 times smaller than the CSS and  $X^3Z^3$  Floquet code thresholds. This is partly explained by noting that the SDEM3 noise model contains measurement errors which give rise to hyperedges in the decoding hypergraphs of the honeycomb codes [15] but only graph-like edges for the CSS and  $X^3Z^3$  Floquet codes [11]. As we explain below, these hyperedges degrade the MWPM decoder performance. As the noise bias increases, the thresholds for both honeycomb codes increase only by  $\leq 6 \times 10^{-4}$ , where the thresholds at the infinite bias are only about 1.03 – 1.08 of their thresholds at the depolarising noise.

We find that there are differences, albeit modest ones, between the performance of the  $XYZ^2$  and  $P^6$  honeycomb codes under biased noise; these differences have not been pointed out before in the literature. While the  $XYZ^2$  honeycomb code has a better performance than the  $P^6$  honeycomb code for the code-capacity noise model, surprisingly we find that its performance is more inferior to that of the  $P^6$  Floquet code for the SDEM3 noise model, considering the similarity of the former to



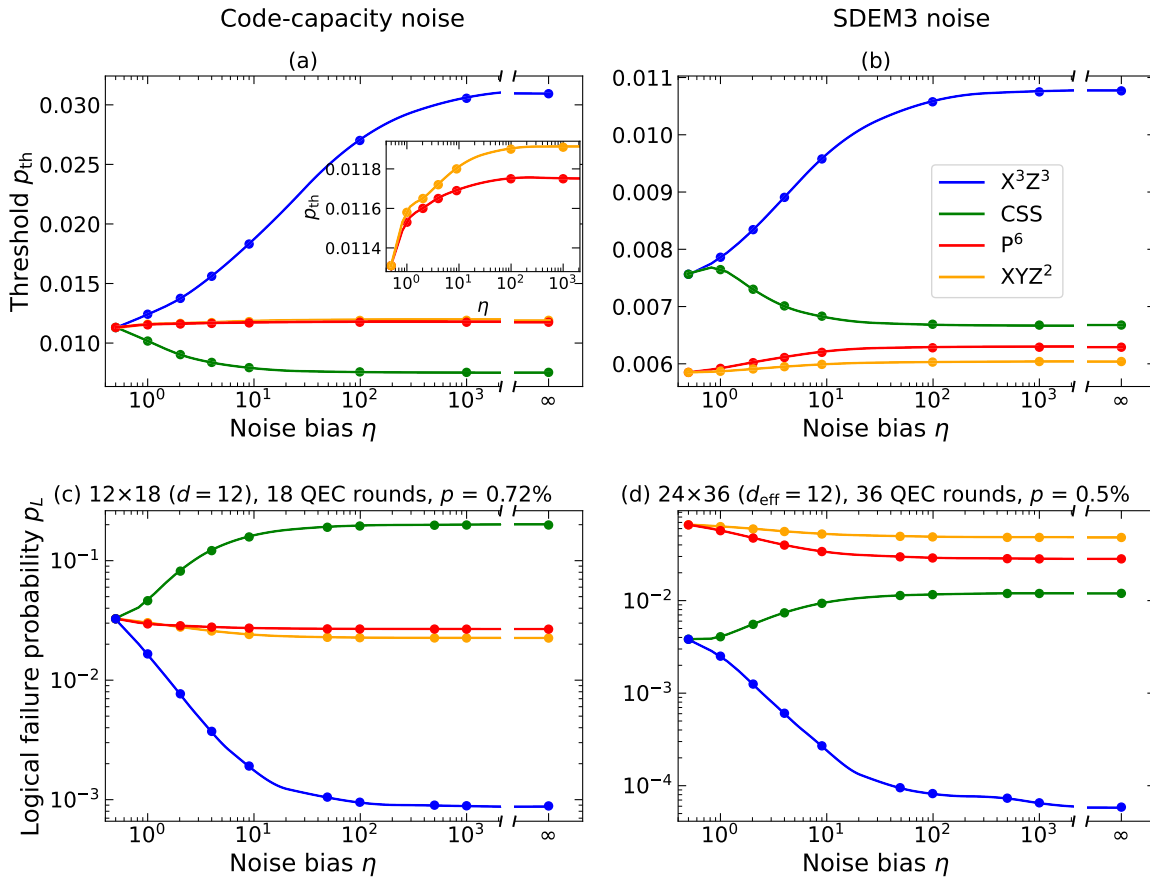


FIG. 6. (a,b) Thresholds ( $p_{th}$ ) and (c,d) sub-threshold logical failure probability  $p_L$  of different Floquet codes as a function of noise bias  $\eta$ . Codes studied are  $X^3Z^3$  (blue), CSS (green),  $P^6$  (red) and  $XYZ^2$  (orange). Results are computed for two different noise models: (a,c) code-capacity and (b,d) SDEM3. (a) Inset: Zoom-in threshold plots for  $P^6$  (red) and  $XYZ^2$  (orange) codes. Lower panels: Results are calculated for code distance (c) Code size  $12 \times 18$  ( $d = 12$ ) with 18 QEC rounds with  $p = 0.72\%$  and (d) Code size  $24 \times 36$  ( $d_{eff} = 12$ ) with 36 QEC rounds with  $p = 0.5\%$ . Each data point is averaged over  $10^6 - 10^9$  shots. For better visualisations, we fit all curves with quadratic splines.

the bias-tailored  $XYZ^2$  static code [40]. However, owing to stabilisers being measured in two measurement sub-rounds, the  $XYZ^2$  Floquet code no longer possesses all the symmetries of the static version making the dynamical code not be able to inherit all the benefits of its static counterpart.

The performance difference between the  $XYZ^2$  and  $P^6$  honeycomb codes can be understood from the distribution of hyperedge-like syndromes (namely, those with four triggered detectors) in the detector hypergraphs under the biased SDEM3 noise model. These hyperedges generally degrade the code's performance when using a matching decoder since they must be decomposed (see Ref. [15] for a detailed description of the decoding in a hyperbolic version of the honeycomb code). In an infinitely biased SDEM3 noise model that includes two-qubit noise but no measurement errors, the  $P^6$  code has hyperedges resulting from only  $Z$  errors occurring after

the red check measurement subrounds, while the  $XYZ^2$  code has hyperedges resulting from certain  $Z$  errors in all subrounds. There is no difference in the overall number of hyperedges in the two hypergraphs. However, one result of this different arrangement of the hyperedges is that two-qubit  $ZZ$  errors can lead to hyperedge syndromes only in the  $XYZ^2$  Floquet code. This is explained in Appendix E. As a result of this, in an infinitely biased regime, where Pauli errors after MPP gates are evenly distributed between  $Z_1$ ,  $Z_2$  and  $Z_1Z_2$ , there are more hyperedge syndromes triggered in the  $XYZ^2$  code than in the  $P^6$  code. To support this conclusion, we can see from Fig. 6(a) that the difference in thresholds between these codes is marginal under the code-capacity noise. Because honeycomb codes are prone to hyperedges error, better performance of the honeycomb codes might be expected using a correlated MWPM decoder such as the one used in Ref. [7].

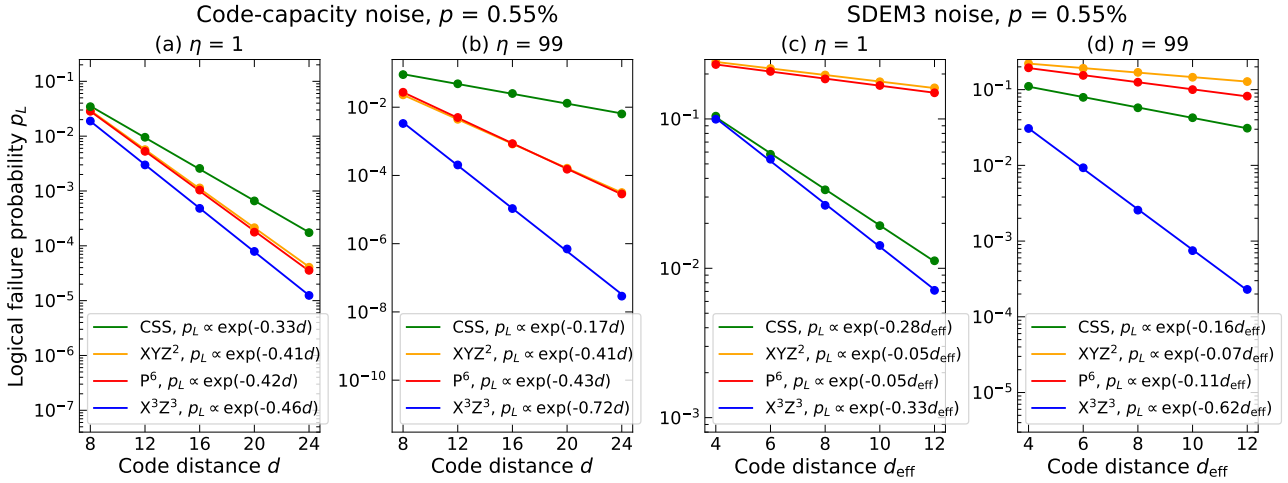


FIG. 7. Exponential suppression of the sub-threshold logical failure probabilities  $p_L$  with respect to  $d_{\text{eff}}$  for different Floquet codes:  $XYZ^2$  (orange),  $P^6$  (red),  $X^3Z^3$  (blue), and CSS (green). The results are calculated for different noise models: (a,b) Code-capacity and (c,d) SDEM3 noise models, with a physical error rate  $p = 0.55\%$ . They are also computed using different bias strengths: (a,c)  $\eta = 1$  and (b,d)  $\eta = 99$ . All curves can be fitted to an exponential decay function  $f \propto \exp(-\gamma d)$  or  $f \propto \exp(-\gamma d_{\text{eff}})$  where  $\gamma$  depends on the bias strength  $\eta$  and is an increasing function of  $(p_{\text{th}} - p)$ . Each data point is averaged over  $10^6 - 10^9$  shots.

As a result of the shift of the thresholds with the noise bias, the subthreshold performance of the codes changes accordingly. As shown in Figs. 6(c) and 6(d), the subthreshold logical failure probability improves significantly for the  $X^3Z^3$  code, while it becomes only slightly better for the honeycomb codes and deteriorates for the CSS code.

Besides the threshold, another quantity that is of interest is the scaling of the code sub-threshold performance with the code distance. To show this, we plot the sub-threshold logical failure probability as a function of  $d$  or  $d_{\text{eff}}$  for varying levels of noise bias in Fig. 7. The logical failure probabilities for all codes decrease exponentially with the code distance, i.e.,  $p_L \propto \exp(-\gamma d)$  or  $p_L \propto \exp(-\gamma d_{\text{eff}})$ . Among all codes presented, the  $X^3Z^3$  code has the largest logical error suppression rate  $\gamma$ . At higher noise bias, this error suppression rate becomes significantly larger for the  $X^3Z^3$  code, moderately increases for the two honeycomb codes and decreases for the CSS Floquet code. The reason is that as the noise bias increases, a fixed subthreshold physical error rate moves relatively with respect to the shifting threshold, so that it becomes much further below the threshold for the  $X^3Z^3$  Floquet code, moves moderately away from the threshold for the two honeycomb codes and becomes closer to the threshold for the CSS code [see Figs. 6(a) and 6(b)].

The error suppression rate  $\gamma$  is related to the error suppression factor  $\Lambda$  proposed in Ref. [7] which is defined as the reduction factor in the logical failure probability as the code distance increases by 2. Mathematically, it is given by  $\Lambda \equiv p_L(d)/p_L(d+2) = \exp(2\gamma)$  for the code-capacity noise and similarly for the SDEM3 noise model but with  $d$  replaced by  $d_{\text{eff}}$ . In Table I of Ap-

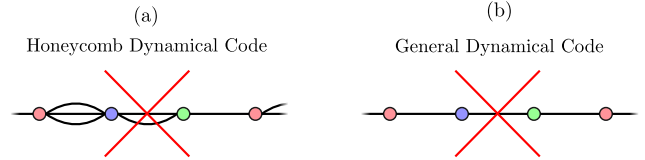


FIG. 8. An illustration of Theorems 1 (a) and 2 (b). We display examples of  $Z$ -detector graphs (edges correspond to  $Z$  errors and vertices to detectors) that are forbidden by these theorems, for HDCs (a) and GDCs (b).

pendix C 2 we list the values of  $\Lambda$  corresponding to the  $\gamma$  values shown in Fig. 7.

## VI. NO-GO THEOREMS FOR 1D DECODING GRAPHS OF DYNAMICAL CODES

As seen in the previous section, although the performance of the  $X^3Z^3$  Floquet codes performance is significantly better compared to other Floquet codes, its threshold at the infinite-bias code-capacity noise does reach the 50% threshold of its bias-tailored static version [36]. To explain this, in the following, we show that there are fewer symmetries in the decoding graphs of dynamical codes which restricts code performance. Indeed, the key feature resulting in the high performance of bias-tailored static codes (that their decoding can be understood as decoding a series of repetition codes [32, 33, 35, 36]), which as we will show below is not possible for dynamical codes built from two-qubit measurements. We argue that due to this limiting constraint, the  $X^3Z^3$  Floquet code likely approaches optimality un-

der infinite bias noise and using a matching decoder, owing to its decoding occurring on a series of disjoint planar graphs. We formalise this by showing that (given reasonable and typical assumptions) the decoding graphs of dynamical codes cannot be decomposed into a collection of one-dimensional (1D) repetition-code decoding graphs, i.e., graphs with maximum degree of 2. For codes defined on the honeycomb lattice, we show that their decoding graphs cannot have a more general property, which we call 1D-decodability. A 1D-decodable decoding graph could still result in better performance for the code than a general planar decoding graph. Hence, the fact that this is not possible suggests that planar graph decoding is optimal for dynamical codes on the honeycomb lattice. We illustrate these restrictions in Fig. 8.

We will start by formalising the above notions via:

**Definition 1.** Let  $V$  be a set of detectors for a dynamical code. For every qubit and every time step (i.e., every fault location in the code)  $(q, t)$ , define a hyperedge  $e_{(q,t)} = (v_1, v_2, \dots)$ , where the  $v_i \in V$  are detectors that return  $-1$  outcomes if a single  $Z$  error at fault location  $(q, t)$  occurs. The **Z-detector hypergraph** (ZDH) is defined as  $G = (V, E)$ , where  $E = \bigcup_{q,t} e_{(q,t)}$  is the set of all hyperedges. A **Z-detector graph** (ZDG) is a Z-detector hypergraph in which all hyperedges are edges (their size is 2).

**Definition 2.** A **1D-decodable** Z-detector graph is one in which all vertices have neighbourhoods of size no greater than 2.

Finally, we define dynamical codes in the following way:

**Definition 3.** A **honeycomb dynamical code** (HDC), with “duration”  $T$  and “detection delay”  $k$ , is a finite-depth measurement circuit acting on qubits of the honeycomb lattice (without boundary). The sets of measurements in the circuit,  $\mathcal{M}_t$  ( $t \in \{1, \dots, T\}$ ), are composed of two-body Pauli measurements along coloured edges (either  $r$ ,  $g$ , or  $b$ , for each time step) of the lattice, performed sequentially on a state stabilised by some group  $\mathcal{S}$ . The HDC obeys the following properties:

- (a) Overlapping measurements in consecutive time steps anti-commute and are supported on different edges,
- (b) Detectors (for time steps  $t > 1$ ) are associated with plaquettes in the lattice (they have support only on qubits around their associated plaquette),
- (c) All single-qubit and non-trivial two-qubit errors occurring in time steps  $1 < t < T - k$  are detectable (a trivial error does not change the evolution of the system), and have syndromes of weight  $> 1$ .

Let us first comment on our definition of an HDC. The chosen properties are very natural. The non-commutativity of consecutive measurement subrounds

ensures “local reversibility” of the code, so as to preserve the information [55] (although note that we do not require the code to have logical qubits in our definition). The requirement that consecutive sets of measurements are supported on different edges is not very restrictive: if two (anti-commuting) measurements act on the same edge in consecutive time steps, we can replace the second with a Clifford gate and commute that to the end of the circuit. This merely changes the bases of subsequent measurements without changing their (anti-)commutation. As a result, we replace the HDC with  $T$  time steps with one with  $T' < T$  time steps. We subtract a constant  $k$  from the final time step  $T$  in point (c) in order to avoid complications due to the final-time boundary, where errors close to this boundary can be detected by “reading out” logical qubits (in a memory experiment). That is, we consider errors occurring in “detection cells” [11] that are completed before time step  $T$ .

Finally, we consider more general codes defined on an arbitrary graph  $G$ .

**Definition 4.** A **general dynamical code** (GDC) is a finite-depth measurement circuit acting on qubits associated with vertices of a graph  $G$ . The sets of measurements  $\mathcal{M}_t$  are two-body Pauli measurements associated with edges of  $G$  (each qubit is in the support of one measurement in each time step), performed sequentially on a state stabilised by some group  $\mathcal{S}$ . A GDC obeys properties (a) and (c) of an HDC.

We will first show that an HDC cannot have a 1D-decodable ZDG and therefore its decoding cannot be equivalent to that of a collection of repetition codes. Note that a repetition code graph not only is 1D-decodable but also has a maximum degree of 2, which means there are no double edges between neighbouring vertices. Here, however, we allow for these double edges in our definition of 1D-decodability, and show that this more general property is also impossible. Such double edges naturally arise in Floquet codes, where they correspond to two-qubit undetectable errors (e.g., edge operators about to be measured).

Using the properties of the HDC as defined above, we now prove the first main theorem of our paper

**Theorem 1.** A honeycomb dynamical code with duration more than  $3k + 4$  (for detection delay  $k$ ) cannot have a 1D-decodable Z-detector graph.

*Proof.* Suppose there are  $T$  time steps and  $n$  qubits in the HDC. Note that we take an error occurring in time step  $t$  to mean that it occurs *after* the measurements in  $\mathcal{M}_t$ . We will first restrict the ZDG: let it contain vertices corresponding to all detectors formed in time steps  $t > 1$ , but only those edges corresponding to *detectable* errors, i.e., those occurring in time steps  $1 < t < T - k$ . The number of vertices in this graph is at most  $n(T - 1)/6$ , since in each time step no detectors can be formed on neighbouring plaquettes (see Lemma 1 in Appendix D),

and we can select at most  $n/6$  non-neighbouring plaquettes on the honeycomb lattice without boundary (corresponding to all plaquettes of a single colour). Meanwhile,  $Z$  errors generate  $n$  edges between each measurement subround, resulting in a total of  $n(T-2-k)$  edges in the ZDG.

Consider the set  $E_t$  of edges corresponding to single-qubit  $Z$  errors from time step  $t$ . The maximum number of edges from  $E_t$  between the same two vertices is 2. To see this, consider a scenario in which we have three or more edges between two vertices. Any pair of them corresponds to a weight-2 undetectable error, since it triggers no detectors. Consider three such undetectable errors:  $Z_i Z_j$ ,  $Z_j Z_l$  and  $Z_i Z_l$ . Since  $i$ ,  $j$  and  $l$  are distinct qubits, one of these errors must be acting on non-adjacent qubits in the lattice, which must be detectable (see Lemma 2 in Appendix D).

Let us now create a bipartition of the qubits into sets  $R$  and  $S$  such that no qubits in  $R$  are adjacent to one another in the honeycomb lattice, and similarly for qubits in  $S$ . This is possible since the honeycomb lattice is bipartite. Let us consider the subgraph of the ZDG that contains only edges corresponding to detectable  $Z$  errors on qubits in  $R$ ,  $\text{ZDG}_R$ .  $\text{ZDG}_R$  contains  $n(T-2-k)/2$  edges. Suppose two vertices are connected in this graph by more than one edge. There is therefore at least one undetectable weight-2 error with support only on qubits in  $R$ . These two errors cannot occur in the same time step, owing to the bipartition of qubits (Lemma 2). Meanwhile, if the errors occur on different qubits, there is once again a non-trivial, undetectable error (they will anti-commute with some future measurements). Hence, they must occur on the same qubit,  $i$ , in different time steps. Since the pair of errors is undetectable, the measurements in between them must commute with  $Z_i$ . Hence, there can only be one such measurement, because consecutive measurements with support on  $i$  anti-commute. Therefore, any two of these errors are separated by one time step and so there can only be two such errors. That is, vertices in  $\text{ZDG}_R$  are only connected by at most two edges. Therefore, there is a spanning subgraph of  $\text{ZDG}_R$  with at least  $\lceil n(T-2-k)/4 \rceil$  edges with no vertices in the subgraph connected by more than one edge.

Therefore, the whole ZDG has a subgraph with  $\lceil n(T-2-k)/4 \rceil$  edges and  $\leq n(T-1)/6$  vertices such that no two vertices are connected by more than one edge. That is, there are many more edges than vertices in this subgraph (recall  $T > 3k+4$ ). Such a graph cannot have all vertices with neighbourhoods of size  $\leq 2$ . The size of the neighbourhood of some vertex in the full ZDG is therefore also greater than 2.  $\square$

This precludes the possibility of an HDC having a collection of repetition code graphs as its ZDG. Therefore, the route towards a large threshold under biased noise is impossible for HDCs. Indeed, for large  $T$ , there will be at least approximately  $nT/(nT/6) = 6$  times as many edges as vertices in the ZDG, and there is a subgraph with  $3/2$

as many edges as vertices without any pair of vertices sharing more than one edge. This means the graph must have many cycles with length at least three edges.

It is clear that the codes examined in this paper obey the properties of an HDC. In particular, any Floquet codes related to the CSS Floquet code by Hadamard gates applied to a subset of the qubits (as is the case for the  $X^3 Z^3$  Floquet code) do not have 1D-decodable ZDGs. The reason we have focused on deformation by Hadamard gates is that  $Z$  errors remain associated with graph-like edges in the deformed code's ZDG, rather than hyperedges. While improved performance is possible for infinitely biased noise that produces hyperedges [32], we do not believe this would be the case for Clifford-deformed CSS Floquet codes owing to the high connectivity of the detector graphs of all Hadamard-deformed versions of the code.

Having defined GDCs, we now prove the second main theorem of our paper:

**Theorem 2.** *A GDC with detection delay  $k$  and duration greater than  $2k+2$  (i.e., a constant) cannot have a  $Z$ -detector graph equivalent to a collection of disjoint repetition codes.*

*Proof.* There are  $n/2$  measurements in a given time step. Regardless of how these measurements form detectors, there can be at most  $n/2$  independent such detectors formed. However, there will in fact be far fewer, because each individual measurement anti-commutes with a measurement from the previous time step and so is random. Therefore, a detector must be formed from at least two measurements within a time step. We assume the GDC has a  $Z$ -detector graph. Each  $Z$ -error occurring in time steps  $1 < t < T-k$  is associated with an edge in the ZDG. Focusing on time steps  $t > 1$ , there are therefore  $< n(T-1)/2$  vertices in the ZDG and  $n(T-2-k)$  edges. With a collection of repetition code graphs,  $V \geq E$ , for vertex (edge) number  $V$  ( $E$ ). Hence,  $T > 2k+2$  implies that the ZDG is not a collection of repetition code graphs.  $\square$

Let us consider the implications of Theorem 2. In static codes, as we have pointed out, this repetition code structure in the decoding problem can lead to 50% code capacity thresholds under infinitely biased noise. In GDCs, we do not expect to see such high thresholds owing to Theorem 2. The reason that static codes perform better than dynamical codes under biased noise is that they obey two separate symmetries under an infinitely-biased code-capacity noise model. There is a spatial symmetry that forces syndromes to appear in pairs along 1D strips of the lattice, but there is also a temporal symmetry: syndromes must appear in pairs within a given time slice. This is because a code-capacity noise model includes no measurement errors. These two symmetries simplify the detector graph into a collection of disjoint repetition code decoding graphs, leading to a high performance of these codes under biased noise. GDCs necessarily break the temporal symmetry (for HDCs, this

is a consequence of Lemma 1), leading to edges between vertices in different time slices of the detector graph even without measurement errors (see Fig. 3). We thus expect such codes can only possess a single symmetry under an infinitely-biased code-capacity noise model, as the  $X^3Z^3$  Floquet code does.

## VII. CONCLUSIONS AND OUTLOOK

In this paper, we introduce the  $X^3Z^3$  Floquet code, the first bias-tailored dynamical code based on two-qubit parity check measurements. We show that, despite having no constant stabilisers, the code has a persistent symmetry under pure dephasing (or pure bit-flip) noise which allows for simplified decoding. This results in a substantially improved threshold and sub-threshold performance under biased noise, when compared to other Floquet codes. We demonstrate the enhanced performance through our simulation results obtained from using a fast matching decoder and a noise model approaching realistic circuit-level noise. Besides the superior performance of the  $X^3Z^3$  Floquet code, our results also demonstrate that there are differences, albeit modest, in the threshold and subthreshold performance of the  $XYZ^2$  and  $P^6$  honeycomb codes under biased noise.

To explain why the  $X^3Z^3$  Floquet code does not reach the same high performance as the bias-tailored static codes, we prove that a dynamical code on the honeycomb lattice (obeying certain assumptions common to standard Floquet codes) cannot have a so-called 1D-decodable  $Z$ -detector graph, the crucial requirement for the high performance of static codes (at least those with

out hyperedge-like syndromes). Despite this limitation, the bias-tailored  $X^3Z^3$  Floquet code has the advantage over its static counterpart in that it requires only lower-weight measurements. Specifically for devices without native two-qubit parity measurements, we devise bias-preserving parity check measurement circuits that allow for high implementation of the code and can be applied to any qubit type. Our work therefore demonstrates that the  $X^3Z^3$  Floquet code is a leading quantum error correction code especially for devices with limited connectivity such as the hexagonal and heavy-hexagonal architectures.

We now give several directions for future work. While in this paper we use multi-Pauli product gates for the parity check measurements which are native to certain architectures (for example, Majorana qubits) we leave for future work the study of the code performance using the bias-preserving parity measurement circuits proposed in Sec. III B. Furthermore, it would also be interesting to investigate the performance of the  $X^3Z^3$  Floquet code using a better decoder (such as a tensor network decoder) and to consider ways of analytically deriving the best achievable thresholds for the  $X^3Z^3$  Floquet code.

## ACKNOWLEDGMENTS

We would like to thank our colleagues at Riverlane, especially Alexandra Moylett, Ophelia Crawford, and György Gehér for helpful discussions. We are also grateful to Ophelia Crawford for her reading and comments on the manuscript. CM would like to thank Benjamin Brown for pointing out a useful circuit for performing next-nearest-neighbour entangling gates.

- 
- [1] P. W. Shor, Scheme for reducing decoherence in quantum computer memory, *Phys. Rev. A* **52**, R2493 (1995).
- [2] P. W. Shor, Fault-tolerant quantum computation, in *Proceedings of 37th conference on foundations of computer science* (IEEE, 1996) p. 56.
- [3] A. R. Calderbank and P. W. Shor, Good quantum error-correcting codes exist, *Phys. Rev. A* **54**, 1098 (1996).
- [4] S. J. Devitt, W. J. Munro, and K. Nemoto, Quantum error correction for beginners, *Reports on Progress in Physics* **76**, 076001 (2013).
- [5] D. Gottesman, Opportunities and challenges in fault-tolerant quantum computation, *arXiv:2210.15844* (2022).
- [6] M. B. Hastings and J. Haah, Dynamically generated logical qubits, *Quantum* **5**, 564 (2021).
- [7] C. Gidney, M. Newman, A. Fowler, and M. Broughton, A fault-tolerant honeycomb memory, *Quantum* **5**, 605 (2021).
- [8] J. Haah and M. B. Hastings, Boundaries for the honeycomb code, *Quantum* **6**, 693 (2022).
- [9] C. Gidney, M. Newman, and M. McEwen, Benchmarking the planar honeycomb code, *Quantum* **6**, 813 (2022).
- [10] M. Davydova, N. Tantivasadakarn, and S. Balasubramanian, Floquet codes without parent subsystem codes, *PRX Quantum* **4**, 10.1103/prxquantum.4.020341 (2023).
- [11] M. S. Kesselring, J. C. Magdalena de la Fuente, F. Thomssen, J. Eisert, S. D. Bartlett, and B. J. Brown, Anyon condensation and the color code, *PRX Quantum* **5**, 010342 (2024).
- [12] O. Higgott and N. P. Breuckmann, Constructions and performance of hyperbolic and semi-hyperbolic floquet codes (2023), *arXiv:2308.03750* [quant-ph].
- [13] A. Dua, N. Tantivasadakarn, J. Sullivan, and T. D. Ellison, Engineering 3d floquet codes by rewinding, *PRX Quantum* **5**, 10.1103/prxquantum.5.020305 (2024).
- [14] J. C. M. de la Fuente, J. Old, A. Townsend-Teague, M. Rispler, J. Eisert, and M. Müller, The xyz ruby code: Making a case for a three-colored graphical calculus for quantum error correction in spacetime (2024), *arXiv:2407.08566* [quant-ph].
- [15] A. Fahimniya, H. Dehghani, K. Bharti, S. Mathew, A. J. Kollár, A. V. Gorshkov, and M. J. Gullans, Fault-tolerant hyperbolic floquet quantum error correcting codes (2024), *arXiv:2309.10033* [quant-ph].
- [16] M. Davydova, N. Tantivasadakarn, S. Balasubramanian, and D. Aasen, Quantum computation from dynamic au-

- tomorphism codes, *Quantum* **8**, 1448 (2024).
- [17] X. Fu and D. Gottesman, Error correction in dynamical codes, arXiv:2403.04163 (2024).
- [18] C. McLauchlan, G. P. Gehér, and A. E. Moylett, Accommodating fabrication defects on floquet codes with minimal hardware requirements (2024), arXiv:2405.15854 [quant-ph].
- [19] A. G. Fowler, M. Mariantoni, J. M. Martinis, and A. N. Cleland, Surface codes: Towards practical large-scale quantum computation, *Phys. Rev. A* **86**, 032324 (2012).
- [20] A. Y. Kitaev, Fault-tolerant quantum computation by anyons, *Annals of physics* **303**, 2 (2003).
- [21] A. Paetznick, C. Knapp, N. Delfosse, B. Bauer, J. Haah, M. B. Hastings, and M. P. da Silva, Performance of planar floquet codes with majorana-based qubits, *PRX Quantum* **4**, 010310 (2023).
- [22] D. Aasen, J. Haah, P. Bonderson, Z. Wang, and M. Hastings, Fault-tolerant hastings-haah codes in the presence of dead qubits (2023), arXiv:2307.03715 [quant-ph].
- [23] B. Hetényi and J. R. Wootton, Tailoring quantum error correction to spin qubits, *Phys. Rev. A* **109**, 032433 (2024).
- [24] A. Somoroff, Q. Ficheux, R. A. Mencia, H. Xiong, R. Kuzmin, and V. E. Manucharyan, Millisecond coherence in a superconducting qubit, *Phys. Rev. Lett.* **130**, 267001 (2023).
- [25] R. Lescanne, M. Villiers, T. Peronin, A. Sarlette, M. Delbecq, B. Huard, T. Kontos, M. Mirrahimi, and Z. Leghtas, Exponential suppression of bit-flips in a qubit encoded in an oscillator, *Nature Physics* **16**, 509–513 (2020).
- [26] A. Grimm, N. E. Frattini, S. Puri, S. O. Mundhada, S. Touzard, M. Mirrahimi, S. M. Girvin, S. Shankar, and M. H. Devoret, Stabilization and operation of a kerr-cat qubit, *Nature* **584**, 205 (2020).
- [27] S. J. Evered, D. Bluvstein, M. Kalinowski, S. Ebadi, T. Manovitz, H. Zhou, S. H. Li, A. A. Geim, T. T. Wang, N. Maskara, *et al.*, High-fidelity parallel entangling gates on a neutral-atom quantum computer, *Nature* **622**, 268 (2023).
- [28] T. Watson, S. Philips, E. Kawakami, D. Ward, P. Scarlino, M. Veldhorst, D. Savage, M. Lagally, M. Friesen, S. Coppersmith, *et al.*, A programmable two-qubit quantum processor in silicon, *Nature* **555**, 633 (2018).
- [29] T. Tantt, W. H. Lim, J. Y. Huang, N. Dumoulin Stuyck, W. Gilbert, R. Y. Su, M. Feng, J. D. Cifuentes, A. E. Seedhouse, S. K. Seritan, *et al.*, Assessment of the errors of high-fidelity two-qubit gates in silicon quantum dots, *Nature Physics* , 1 (2024).
- [30] D. Aasen, M. Hell, R. V. Mishmash, A. Higginbotham, J. Danon, M. Leijnse, T. S. Jespersen, J. A. Folk, C. M. Marcus, K. Flensberg, and J. Alicea, Milestones toward majorana-based quantum computing, *Phys. Rev. X* **6**, 031016 (2016).
- [31] O. Higgott, T. C. Bohdanowicz, A. Kubica, S. T. Flammia, and E. T. Campbell, Improved decoding of circuit noise and fragile boundaries of tailored surface codes, *Phys. Rev. X* **13**, 031007 (2023).
- [32] D. K. Tuckett, S. D. Bartlett, and S. T. Flammia, Ultra-high error threshold for surface codes with biased noise, *Phys. Rev. Lett.* **120**, 050505 (2018).
- [33] D. K. Tuckett, A. S. Darmawan, C. T. Chubb, S. Bravyi, S. D. Bartlett, and S. T. Flammia, Tailoring surface codes for highly biased noise, *Phys. Rev. X* **9**, 041031 (2019).
- [34] D. K. Tuckett, S. D. Bartlett, S. T. Flammia, and B. J. Brown, Fault-tolerant thresholds for the surface code in excess of 5% under biased noise, *Phys. Rev. Lett.* **124**, 130501 (2020).
- [35] J. P. Bonilla Ataides, D. K. Tuckett, S. D. Bartlett, S. T. Flammia, and B. J. Brown, The xzxx surface code, *Nature Communications* **12**, 2172 (2021).
- [36] K. Tiurev, A. Pesah, P.-J. H. Derks, J. Roffe, J. Eisert, M. S. Kesselring, and J.-M. Reiner, Domain wall color code, *Physical Review Letters* **133**, 10.1103/physrevlett.133.110601 (2024).
- [37] A. Dua, A. Kubica, L. Jiang, S. T. Flammia, and M. J. Gullans, Clifford-deformed surface codes, *PRX Quantum* **5**, 10.1103/prxquantum.5.010347 (2024).
- [38] Q. Xu, N. Mannucci, A. Seif, A. Kubica, S. T. Flammia, and L. Jiang, Tailored xzxx codes for biased noise, *Phys. Rev. Res.* **5**, 013035 (2023).
- [39] J. F. San Miguel, D. J. Williamson, and B. J. Brown, A cellular automaton decoder for a noise-bias tailored color code, *Quantum* **7**, 940 (2023).
- [40] B. Srivastava, A. Frisk Kockum, and M. Granath, The  $XYZ^2$  hexagonal stabilizer code, *Quantum* **6**, 698 (2022).
- [41] J. Roffe, L. Z. Cohen, A. O. Quintavalle, D. Chandra, and E. T. Campbell, Bias-tailored quantum ldpc codes, *Quantum* **7**, 1005 (2023).
- [42] J. Claes, J. E. Bourassa, and S. Puri, Tailored cluster states with high threshold under biased noise, *npj Quantum Information* **9**, 9 (2023).
- [43] E. Huang, A. Pesah, C. T. Chubb, M. Vasmer, and A. Dua, Tailoring three-dimensional topological codes for biased noise, *PRX Quantum* **4**, 030338 (2023).
- [44] B. Hetényi and J. R. Wootton, Creating entangled logical qubits in the heavy-hex lattice with topological codes (2024), arXiv:2404.15989 [quant-ph].
- [45] C. Chamberland, G. Zhu, T. J. Yoder, J. B. Hertzberg, and A. W. Cross, Topological and subsystem codes on low-degree graphs with flag qubits, *Phys. Rev. X* **10**, 011022 (2020).
- [46] E. Dennis, A. Kitaev, A. Landahl, and J. Preskill, Topological quantum memory, *Journal of Mathematical Physics* **43**, 4452–4505 (2002).
- [47] O. Higgott and C. Gidney, Sparse blossom: correcting a million errors per core second with minimum-weight matching (2023), arXiv:2303.15933 [quant-ph].
- [48] T. Karzig, C. Knapp, R. M. Lutchny, P. Bonderson, M. B. Hastings, C. Nayak, J. Alicea, K. Flensberg, S. Plugge, Y. Oreg, C. M. Marcus, and M. H. Freedman, Scalable designs for quasiparticle-poisoning-protected topological quantum computation with majorana zero modes, *Phys. Rev. B* **95**, 235305 (2017).
- [49] S. Puri, L. St-Jean, J. A. Gross, A. Grimm, N. E. Frattini, P. S. Iyer, A. Krishna, S. Touzard, L. Jiang, A. Blais, S. T. Flammia, and S. M. Girvin, Bias-preserving gates with stabilized cat qubits, *Science Advances* **6**, 10.1126/sciadv.aay5901 (2020).
- [50] P. Krantz, M. Kjaergaard, F. Yan, T. P. Orlando, S. Gustavsson, and W. D. Oliver, A quantum engineer’s guide to superconducting qubits, *Applied physics reviews* **6**, 10.1063/1.5089550 (2019).
- [51] C. D. Bruzewicz, J. Chiaverini, R. McConnell, and J. M. Sage, Trapped-ion quantum computing: Progress and challenges, *Applied Physics Reviews* **6**, 10.1063/1.5088164 (2019).
- [52] G. Burkard, T. D. Ladd, A. Pan, J. M. Nichol, and J. R.

- Petta, Semiconductor spin qubits, *Rev. Mod. Phys.* **95**, 025003 (2023).
- [53] K. Wintersperger, F. Dommert, T. Ehmer, A. Houranov, J. Klepsch, W. Maurer, G. Reuber, T. Strohm, M. Yin, and S. Luber, Neutral atom quantum computing hardware: performance and end-user perspective, *EPJ Quantum Technology* **10**, 32 (2023).
- [54] C. Gidney, Stim: a fast stabilizer circuit simulator, *Quantum* **5**, 497 (2021).
- [55] D. Aasen, J. Haah, Z. Li, and R. S. K. Mong, Measurement quantum cellular automata and anomalies in floquet codes (2023), arXiv:2304.01277 [quant-ph].
- [56] J. W. Harrington, *Analysis of quantum error-correcting codes: symplectic lattice codes and toric codes*, PhD thesis, California Institute of Technology, Pasadena, California (2004).

## Appendix A: Details of honeycomb and CSS Floquet codes

### 1. Honeycomb code

We here provide details of the two honeycomb code variants discussed in the main text. The codes' logical operators evolve through their measurement cycles. In Fig. 9(a), we show one set of logical operators evolving through two measurement cycles. While the measurement sequence has period 3, the logical operators only return to their initial values (up to signs) with period 6.

In Fig. 9(b) we show the plaquette and edge operators for both honeycomb code variants. The  $P^6$  code has edge operators with Pauli bases defined by the edge colour, while the  $XYZ^2$  code has edge operators with bases defined by the edge's orientation and position relative to neighbouring plaquettes [see Fig. 9(b)]. The plaquette operators of the  $P^6$  code also differ between plaquettes of different colours, while the plaquette operators of the  $XYZ^2$  code are all the same. These plaquette operators are products of edge operators along the boundary of the plaquette. For example, a red plaquette operator in the  $P^6$  code is the product of the green and blue  $YY$  and  $ZZ$  (respectively) edge operators around its boundary. We measure plaquette operators in two rounds. For example, after measuring  $g \rightarrow b$  checks, we can learn the value of an  $X$  plaquette by multiplying the measurement values of green and blue checks around its boundary. Unlike the CSS and  $X^3Z^3$  Floquet codes, the honeycomb code has constant plaquette stabilisers.

### 2. CSS Floquet code

In Fig. 10, we illustrate the measurement cycle of the CSS Floquet code and the resulting evolution of (one set of) its logical operators. Its logical operators are either of  $X$ -type or  $Z$ -type for all time, as shown. We show an  $X$ -type logical operator defined on a vertical non-trivial cycle of the lattice. However, there exists another  $Z$ -

type logical operator (not shown) defined on that same vertical cycle. One can find this operator (and its anti-commuting partner) by noting the symmetry in the code obtained by proceeding forward by three measurement subrounds ( $t \mapsto t + 3$ ) and applying a Hadamard gate to all qubits ( $X \leftrightarrow Z$ ).

The plaquette operator members of the ISG at each step of the measurement cycle are indicated in Fig. 10. As can be seen, after each measurement subround, plaquettes of one colour host only a single ( $X$ - or  $Z$ -type) member of the ISG. To consider detectors, let us follow a single blue  $X$  plaquette through the measurement sequence. After red  $X$  checks (top left of Fig. 10), the plaquette operator is measured (we infer its outcome by multiplying together the check measurement outcomes around its boundary). This initialises the plaquette. It is only then re-measured after green  $X$  check measurements, at which point a detector is formed. After this, blue  $Z$  checks are measured, which anti-commute with the plaquette operator and its subsequent measurement outcomes are random.

## Appendix B: Noise models

In this paper, we consider two different noise models: code-capacity and entangling measurement (SDEM3) noise models. In the code-capacity noise model, we apply single-qubit Pauli noise on all the data qubits independently at every measurement subround. The single-qubit Pauli noise channel is given by

$$\mathcal{E}_{1q}(\rho) = (1 - p)\rho + p_X \hat{X}\rho\hat{X} + p_Y \hat{Y}\rho\hat{Y} + p_Z \hat{Z}\rho\hat{Z}. \quad (\text{B1})$$

Here,  $p \equiv p_X + p_Y + p_Z$  is the total error probability. As in the literature, we define the noise bias as  $\eta = p_Z/(p_X + p_Y)$  and assume  $p_X = p_Y$ . Several values of  $\eta$  are worth listing:

1.  $\eta = 0 \rightarrow p_Z = 0$ , and  $p_X = p_Y = p/2$ ,
2.  $\eta = 0.5 \rightarrow p_X = p_Y = p_Z = p/3$ ,
3.  $\eta = \infty \rightarrow p_Z = p$ , and  $p_X = p_Y = 0$ .

Besides the code-capacity noise model, in this paper we also use the SDEM3 noise model which assume noisy multi-qubit Pauli product measurement (MPP) gates. The SDEM3 noise model applies single-qubit noise after every single-qubit gate, reset and measurement, two-qubit noise after each MPP gate, and a random classical flip after every measurement. We assume each of the error channels occurs with a total probability  $p$ , as in Ref. ???. To take into account biased noise, we generalise the SDEM3 depolarising noise model used in Refs. [9, 18]. Here the single-qubit noise channel has the same form as given in Eq. (B1) for the code-capacity noise model.

On top of the single-qubit errors, this model also has a two-qubit noise channel given by

$$\mathcal{E}_{2q}(\rho) = (1 - p)\rho + \sum_{O \in \{I, X, Y, Z\}^{\otimes 2} \setminus \{I \otimes I\}} p_O \hat{O}\rho\hat{O}, \quad (\text{B2})$$

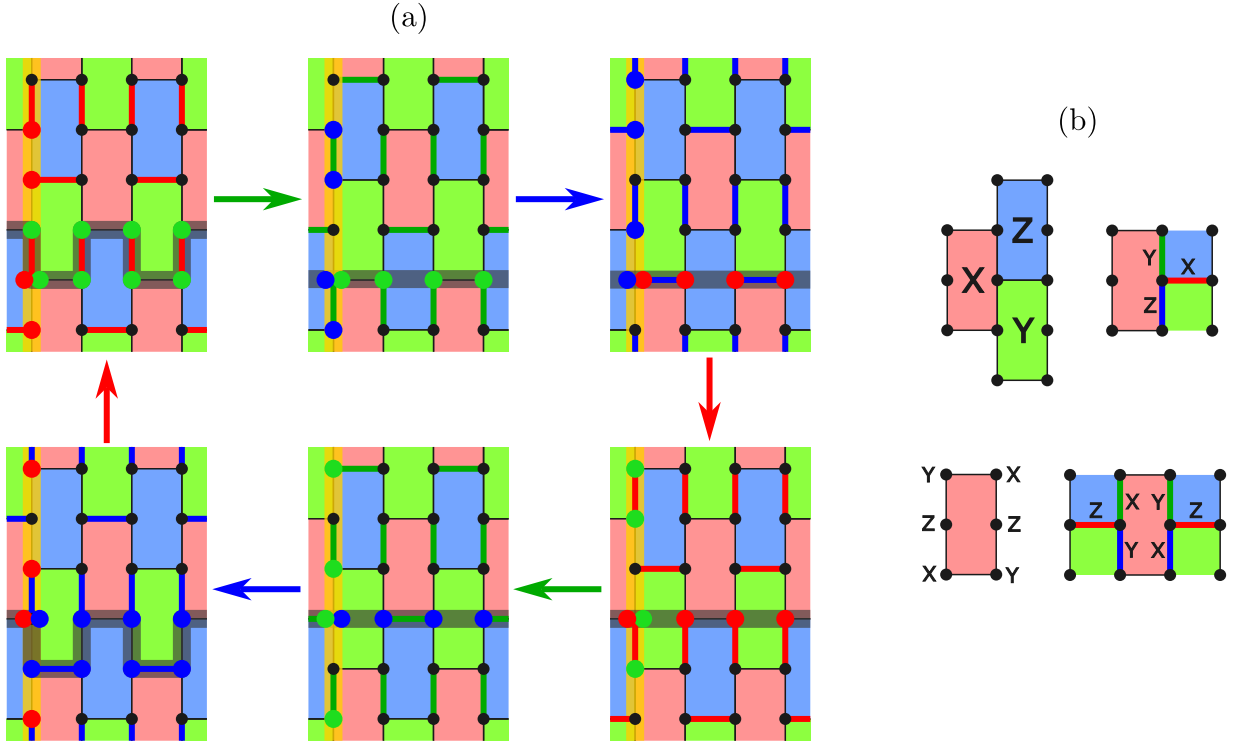


FIG. 9. The honeycomb code measurement cycle, logical operators, plaquettes and edges. (a) A distance-4 (under code-capacity noise)  $P^6$  code [7] is shown throughout its evolution. Edge check measurements are defined in (b). One set of anti-commuting logical operators is shown: a vertical logical defined on the yellow-shaded non-trivial cycle of the torus, and a horizontal logical defined on the grey-shaded non-trivial cycle. The logicals are defined as the product of Pauli operators on coloured qubits in the cycle, where red, green and blue qubits support  $X$ ,  $Y$ , and  $Z$  Pauli bases, respectively. The other set of logical operators is offset by three measurement subrounds. (b) Top: The plaquette operators of the  $P^6$  honeycomb code are shown along with the edge operators measured (red, green and blue edges/plaquettes support  $X$ ,  $Y$  and  $Z$  operators, respectively). Bottom: All plaquette operators of the  $XYZ^2$  honeycomb model are the same and are shown on the left. Edge operators are defined based on their orientation in the T junction (rather than edge colour), as shown on the right.

which is applied after each of the MPP gates. To conform with how the bias is defined for the single-qubit noise channels, we also use  $\eta$  to characterize the bias of the two-qubit noise channel. Specifically, we define the bias  $\eta$  for the two-qubit noise channel such that

1.  $\eta = 0 \rightarrow p_{ZZ} = p_{IZ} = p_{ZI} = 0$  and each of the other probabilities is  $p/12$ ,
2.  $\eta = 0.5 \rightarrow$  each of the Pauli errors occurs with  $p/15$ , and
3.  $\eta = \infty \rightarrow p_{ZZ} = p_{IZ} = p_{ZI} = p/3$ , and the other probabilities are 0.

Just as for the single-qubit noise, the above definition of  $\eta$  ensures that the two-qubit noise at three special points  $\eta = 0$ ,  $\eta = 0.5$  and  $\eta = \infty$  has the required forms (no  $Z$  errors, depolarising, and pure dephasing, respectively). Given that the two-qubit error probabilities at these  $\eta$  values must satisfy the conditions above, we define  $\zeta \in$

$[0, 1]$  and write the two-qubit Pauli error probabilities as

$$\begin{aligned} p_{ZZ} = p_{ZI} = p_{IZ} &= \zeta p/3, \\ p_O &= (1 - \zeta)p/12, \\ \text{for } O \in \{I, X, Y, Z\}^{\otimes 2} \setminus \{II, ZI, IZ, ZZ\}, \end{aligned} \quad (\text{B3})$$

with  $\eta$  and  $\zeta$  related via:

$$\zeta = \frac{3}{5} \left( \frac{\eta}{1 + \eta} \right)^2 + \frac{2}{5} \left( \frac{\eta}{1 + \eta} \right). \quad (\text{B4})$$

Note that Eq. (B3) is defined such that the total probability of all the Pauli errors  $\sum_{O \in \{I, X, Y, Z\}^{\otimes 2} \setminus \{I \otimes I\}} p_O = p$  regardless of the noise bias  $\eta$ . Apart from the single- and two-qubit Pauli noise channels, we also apply a classical flip of the measurement results with probability  $p$  after each of the single and two-qubit measurements. These measurement flips are uncorrelated with the single and two-qubit noise channels.



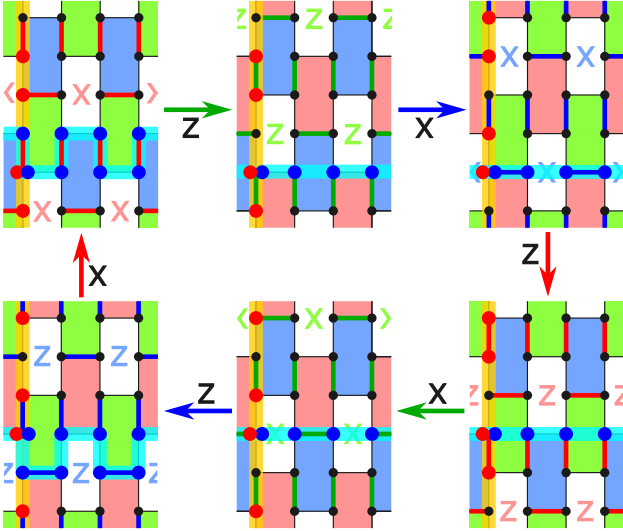


FIG. 10. Measurement cycle for the CSS Floquet code.  $X$  or  $Z$  edge operators are measured in each time step, with the colour of edge and Pauli type indicated by the labelled arrows. Plaquettes labelled with  $X$  or  $Z$  labels host only a stabiliser operator of the corresponding type, while other plaquettes host both  $X$ - and  $Z$ -type stabilisers. One set of anti-commuting logical operators is shown.

### Appendix C: Details of numerical simulations

For each distance  $d_{\text{eff}} = d/2$  (where  $d_{\text{eff}}$  and  $d$  are the minimum number of fault locations required to produce a logical error for the SDEM3 and code-capacity depolarising noise models, respectively), we construct a  $2d_{\text{eff}} \times 3d_{\text{eff}}$  honeycomb lattice with periodic boundary conditions. We run quantum memory experiments for  $3d_{\text{eff}}$  QEC rounds or  $18d_{\text{eff}}$  measurement subrounds (1 QEC round consists of 6 measurement subrounds). We choose a single logical qubit for each Floquet code (they all encode two logical qubits on a lattice with periodic boundary conditions) to test for the logical failure probability. Depending on the codes and parameter regimes, we run different numbers of Monte Carlo shots ranging from  $10^6 - 10^{10}$  for each of the horizontal and vertical logical observables, which give us the horizontal  $p_H$  and vertical  $p_V$  logical failure probabilities. We then report the combined logical error probability:

$$p_L = 1 - (1 - p_H)(1 - p_V), \quad (\text{C1})$$

which is an estimate of the probability that *either* a vertical or a horizontal logical error occurs. Equation (C1) assumes that the horizontal and vertical logical errors occur independently. We run the simulations of the four different Floquet codes for different values of physical error rates  $p$  with various strengths of noise bias  $\eta$  and under the two different noise models.

	Code-capacity		SDEM3	
	$\eta = 1$	$\eta = 99$	$\eta = 1$	$\eta = 99$
CSS	1.94	1.39	1.74	1.37
XYZ <sup>2</sup>	2.27	2.28	1.11	1.15
P <sup>6</sup>	2.31	2.37	1.12	1.24
X <sup>3</sup> Z <sup>3</sup>	2.49	4.26	1.94	3.42

TABLE I. Error suppression factors  $\Lambda$  for different Floquet codes calculated using two different noise models, code-capacity and SDEM3, with varying levels of noise bias  $\eta$ . Results are calculated with a physical error rate  $p = 0.55\%$ . The lambda factor is related to the error suppression rate  $\gamma$  shown in Fig. 7

### 1. Thresholds

To extract thresholds for the codes at various noise-bias strengths, we perform a fit of the data to the curve  $A + Bx + Cx^2$  where  $x = (p - p_{\text{th}})d^{1/\nu}$  or  $x = (p - p_{\text{th}})d_{\text{eff}}^{1/\nu}$  for the code-capacity and SDEM3 noise models, respectively. Here,  $\nu$  is the critical exponent,  $p_{\text{th}}$  is the Pauli threshold and  $A, B, C$  are the fit parameters [56]. Figures 11, 12, 13 and 14 show the resulting data collapse and close-to-threshold plots for various bias strengths for the X<sup>3</sup>Z<sup>3</sup>, CSS, P<sup>6</sup> and XYZ<sup>2</sup> Floquet codes, respectively.

### 2. Error suppression factor

In Table I, we list the values of the error suppression factor  $\Lambda$  which are calculated from the error suppression rate  $\gamma$  shown in Fig. 7.

### Appendix D: Details of the no-go theorems for 1D decoding of dynamical codes

**Lemma 1.** *In a honeycomb dynamical code, at each time step  $t > 1$ , no detectors can be formed on neighbouring plaquettes.*

*Proof.* Suppose that neighbouring plaquettes  $F_1$  and  $F_2$  are coloured red and blue, respectively, and they both host detectors in time step  $t > 1$ . Let  $\mathcal{D}_1, \mathcal{D}_2 \subset \mathcal{M}_t$  be the sets of measurements from  $\mathcal{M}_t$  belonging to the detectors at  $F_1$  and  $F_2$ , respectively. That is, the measurements in  $\mathcal{D}_j$  act only on qubits around  $F_j$ .  $\mathcal{M}_t$  contains measurements along edges of a particular colour. Hence, it must be made up of measurements on green edges, since each red and blue edge has overlap with two red or two blue plaquettes, respectively, and either  $\mathcal{D}_1$  or  $\mathcal{D}_2$  would have to be empty—a contradiction.

For there to be detectors at both plaquettes, we require that, for all  $M \in \mathcal{M}_{t-1}$ ,  $[M, \prod_{D \in \mathcal{D}_j} D] = 0$ , for  $j = 1, 2$ . Otherwise the plaquette operator outcomes would be random. However, from the assumptions of a HDC, for each  $D \in \mathcal{D}_1$ , there is a measurement in  $\mathcal{M}_{t-1}$  that

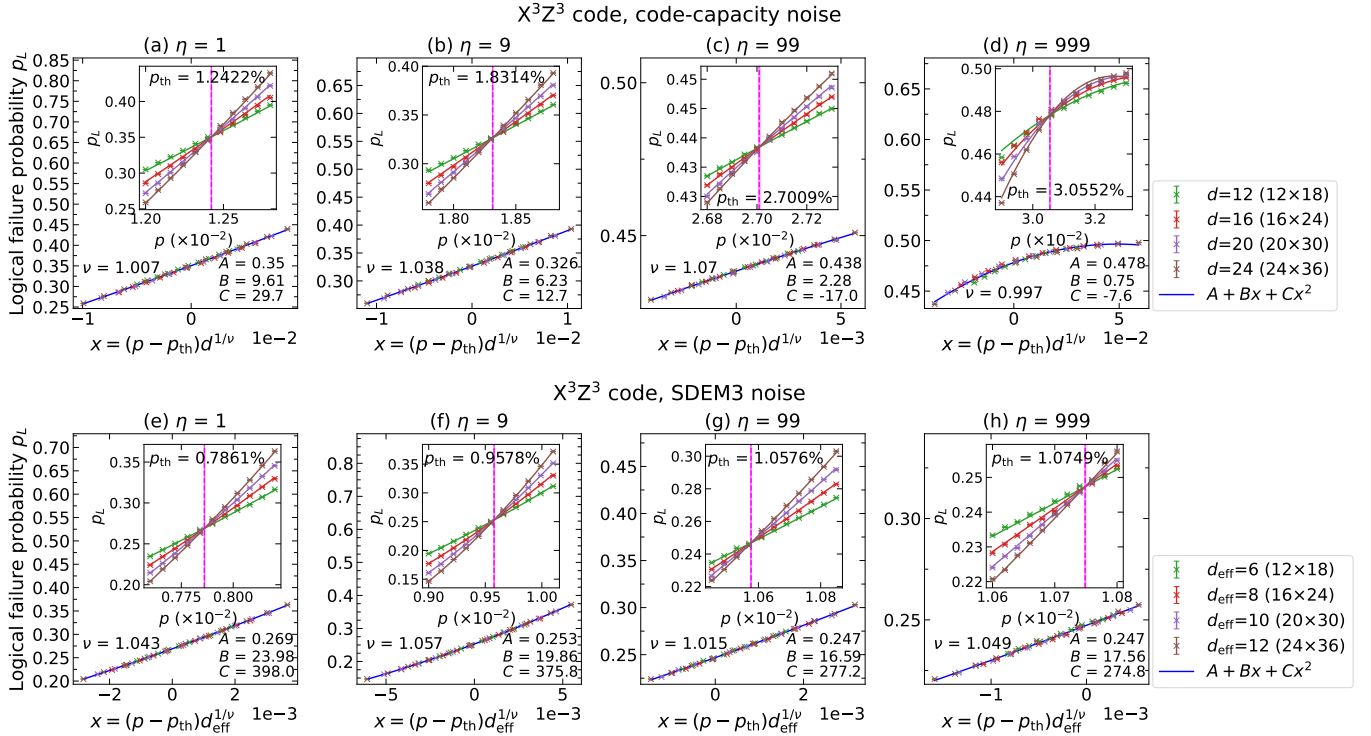


FIG. 11. Logical failure probability  $p_L$  of the  $X^3Z^3$  Floquet code as a function of  $x = (p - p_{th})d^{1/\nu}$  or  $x = (p - p_{th})d_{eff}^{1/\nu}$  for different noise models: Code capacity (upper panels) and SDEM3 (lower panels), with various bias strengths: (a,e)  $\eta = 1$ , (b,f)  $\eta = 9$ , (c,g)  $\eta = 99$ , and (d,h)  $\eta = 999$ . We fit the results to the function  $A + Bx + Cx^2$  (blue line). Insets: Logical failure probability  $p_L$  vs physical error rate  $p$ ; thresholds  $p_{th}$  are shown by the magenta vertical lines. Results for each distance  $d$  and physical error rate  $p$  are averaged over  $10^6 - 10^7$  number of shots.

anti-commutes with it. Therefore,  $\prod_{D \in \mathcal{D}_j} D$  has even overlap with all edges that support measurements from  $\mathcal{M}_{t-1}$ , for  $j = 1, 2$ . The only way for this to occur for both  $j = 1, 2$  is if all  $M \in \mathcal{M}_{t-1}$  are also on green edges (if they are supported on red edges, one will have odd overlap with each  $D \in \mathcal{D}_1$ , and similarly for  $D \in \mathcal{D}_2$  if they are supported on blue edges). This contradicts property (a) of Definition 3.  $\square$

**Lemma 2.** *Two  $Z$  errors occurring in the same time step  $t$  ( $1 < t < T - k$ ) on non-adjacent qubits in the honeycomb lattice are detectable in a honeycomb dynamical code.*

*Proof.* Consider the error  $Z_i Z_j$ , where qubits  $i$  and  $j$  are non-adjacent. If this error were undetectable, then  $Z_i Z_j$  would stabilise the state of the system at time  $t$  or it would be absorbed by future measurements. If it is a stabiliser, then it commutes with all measurements in  $\mathcal{M}_t$ . It is not a member of  $\mathcal{M}_t$ , since  $Z_i Z_j$  is not an edge operator. Hence it must also stabilise the state of the system at time step  $t - 1$ . Note also there is one measurement from  $\mathcal{M}_t$  that acts as  $Z$  on qubit  $i$  (since  $i$  and  $j$  belong to separate edges of the lattice). But then consider the measurement from  $\mathcal{M}_{t-1}$  that has support on qubit  $i$ , which must anti-commute with  $Z_i$  and hence

also anti-commute with  $Z_i Z_j$ . Therefore, this operator is not a stabiliser of the state at time  $t$ . It also must anti-commute with some future measurement in  $\mathcal{M}_{t+1}$  or  $\mathcal{M}_{t+2}$  for the same reason and hence it is not absorbed by future measurements. Since this error flips future measurements and is not a stabiliser, it is non-trivial and hence is detectable [property (c) of HDCs].  $\square$

## Appendix E: Hyperedge errors in honeycomb codes under infinite noise bias

The honeycomb code variants, unlike the CSS and  $X^3Z^3$  Floquet codes (ignoring  $Y$  errors), experience errors that produce hyperedge syndromes [15, 17], even in the infinitely biased regime. These hyperedges degrade the performance of a matching decoder as they must be decomposed into edges, thereby losing some information about the correlations between detectors. In the honeycomb code, these hyperedges can be formed from single-qubit  $Z$  errors, as shown in Fig. 15.

Consider, to begin with, the  $P^6$  honeycomb code. A single-qubit  $Z$  error on this code can only result in a hyperedge syndrome (four flipped detectors) if it occurs between  $R$  and  $G$  check measurements. This hyperedge is highlighted in red in Fig. 15(a). Otherwise a  $Z$  error

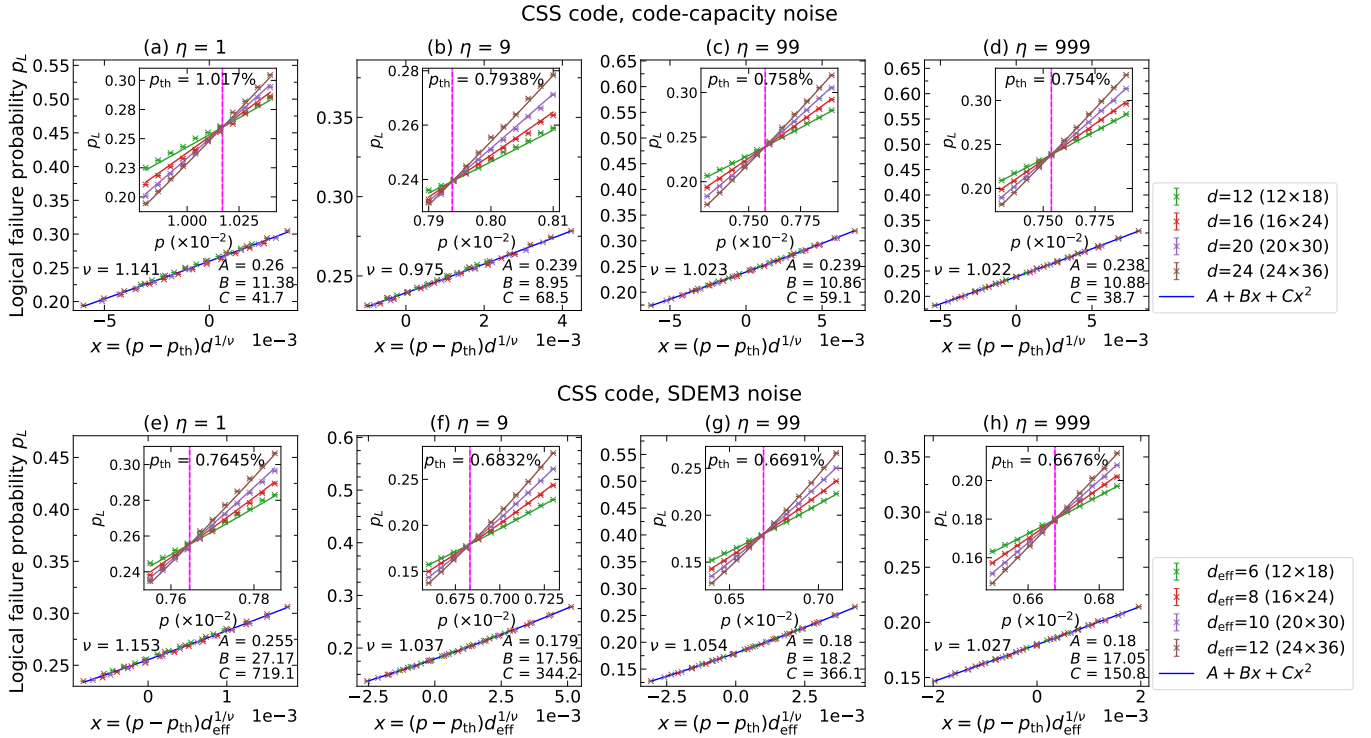


FIG. 12. Logical failure probability  $p_L$  of the CSS Floquet code as a function of  $x = (p - p_{\text{th}})d^{1/\nu}$  or  $x = (p - p_{\text{th}})d_{\text{eff}}^{1/\nu}$  for different noise models: Code capacity (upper panels) and SDEM3 (lower panels), with various bias strengths: (a,e)  $\eta = 1$ , (b,f)  $\eta = 9$ , (c,g)  $\eta = 99$ , and (d,h)  $\eta = 999$ . We fit the results to the function  $A + Bx + Cx^2$  (blue line). Insets: Logical failure probability  $p_L$  vs physical error rate  $p$ ; thresholds  $p_{\text{th}}$  are shown by the magenta vertical lines. Results for each distance  $d$  and physical error rate  $p$  are averaged over  $10^6$  number of shots.

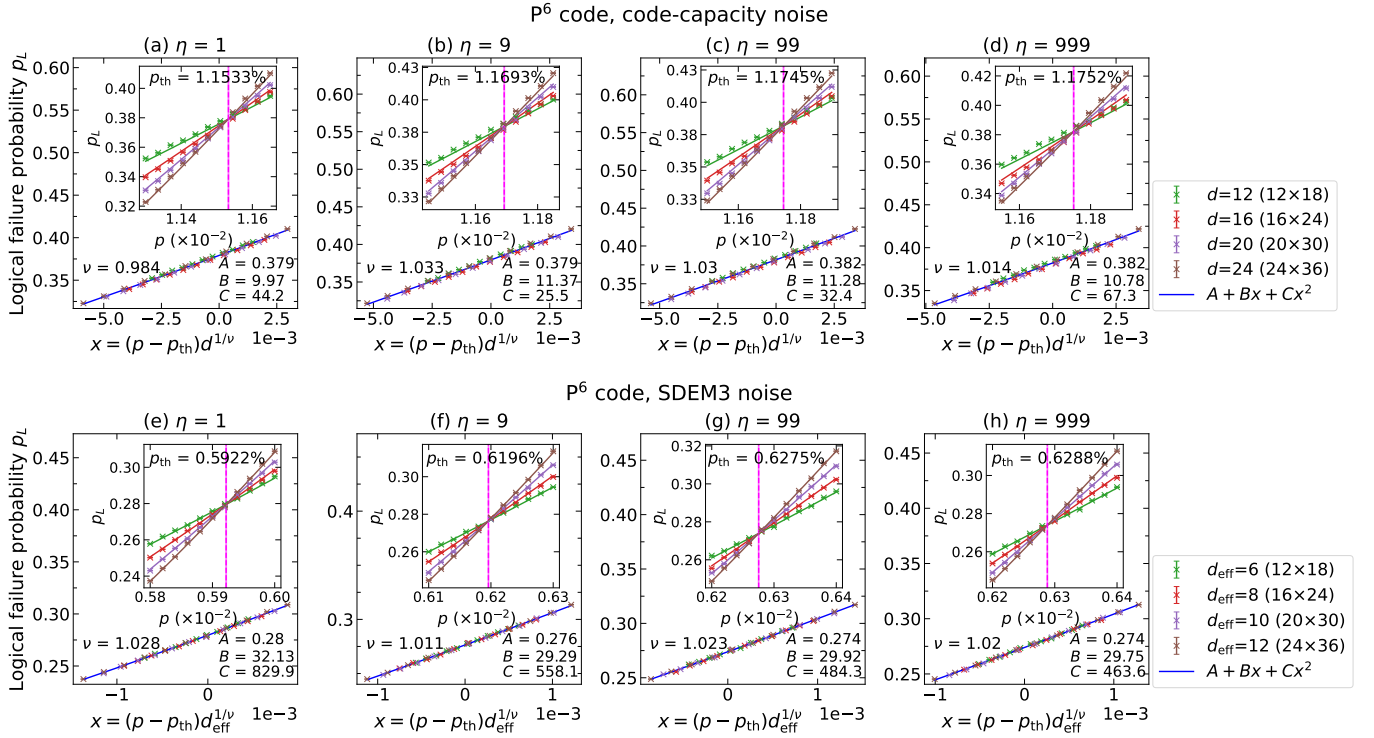
results in an edge-like syndrome (two flipped detectors), shown in blue/green in Fig. 15(a). Notice that the product of the two  $Z$  errors occurring simultaneously results in a graph-like syndrome whenever the error occurs. This is the same for all  $ZZ$  errors occurring along edges in the lattice. In particular,  $ZZ$  errors directly after MPP gates, which occur in the SDEM3 biased-noise model, correspond to edges in the detector hypergraph.

In the  $XYZ^2$  honeycomb code, by contrast, hyperedges can be formed from  $Z$  errors occurring at any time step (although not from any location and time step). That is, a  $Z$  error with coordinates  $(x, y, t)$  could form a hyperedge syndrome for any  $t$ , given suitably chosen  $x$  and  $y$ . Two such  $Z$  errors and their syndromes for different time steps are shown in Fig. 15(b). As can be seen, one  $Z$  error produces a hyperedge if it occurs after an  $R$  round, while the other does so only after a  $G$  round. As such, a  $ZZ$  error occurring at a given time may produce a hyperedge syndrome. For example, if the  $ZZ$  error shown (supported by a green edge) in Fig. 15(b) occurs after green MPP measurements, the resulting syndrome will include four detectors.

### Appendix F: $X^3Z^3$ Floquet code with twisted boundary condition

Here we present simulation results obtained for the  $X^3Z^3$  code with twisted boundary conditions. The twisted boundary refers to the case where the qubits at the top row of the honeycomb lattice are connected to qubits at the bottom row, shifted by two columns (see Fig. 16). In the figure, we also show two (of the four) logical operators. The light blue logical operator, which consists of only  $Z$  operators, has a length that scales quadratically with the length of the untwisted code (cf. Fig. 1(c)). As a result, the performance of the twisted code near infinite bias is expected to be better than the untwisted code since it will be harder for the pure dephasing error to form such a long logical operator.

To support this argument, we present the thresholds of such a code in Fig. 17, where we compare them to the thresholds of the untwisted code. The results here are calculated under a code capacity noise model. Data used to obtain the thresholds are presented in Fig. 18. As shown in Fig. 17, only in the regime close to the infinite bias, the twisted code has better thresholds than the untwisted code. For the small noise bias regime ( $\eta \lesssim 10$ ), the thresholds of the twisted code are roughly similar to the those of the untwisted code. However, in the inter-



mediate bias regime, the thresholds of the twisted code are lower than those of the untwisted code. We would

like to note that there is a stronger finite-size effect for the twisted code compared to the untwisted one as can be seen from the Harrington fit plots in Fig. 18.

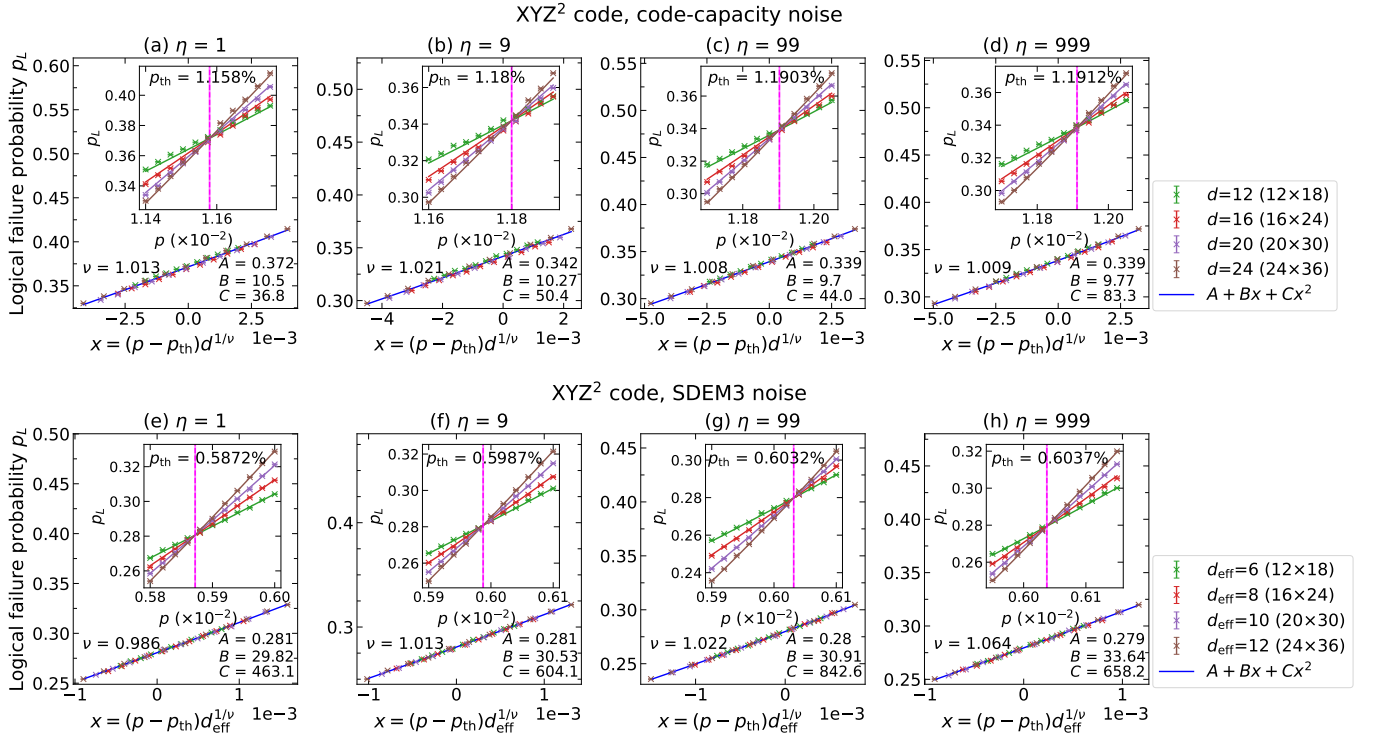


FIG. 14. Logical failure probability  $p_L$  of the XYZ<sup>2</sup> honeycomb code as a function of  $x = (p - p_{\text{th}})d^{1/\nu}$  or  $x = (p - p_{\text{th}})d_{\text{eff}}^{1/\nu}$  for different noise models: Code capacity (upper panels) and SDEM3 (lower panels), with various bias strengths: (a,e)  $\eta = 1$ , (b,f)  $\eta = 9$ , (c,g)  $\eta = 99$ , and (d,h)  $\eta = 999$ . We fit the results to the function  $A + Bx + Cx^2$  (blue line). Insets: Logical failure probability  $p_L$  vs physical error rate  $p$ ; thresholds  $p_{\text{th}}$  are shown by the magenta vertical lines. Results for each distance  $d$  and physical error rate  $p$  are averaged over  $10^6$  number of shots.

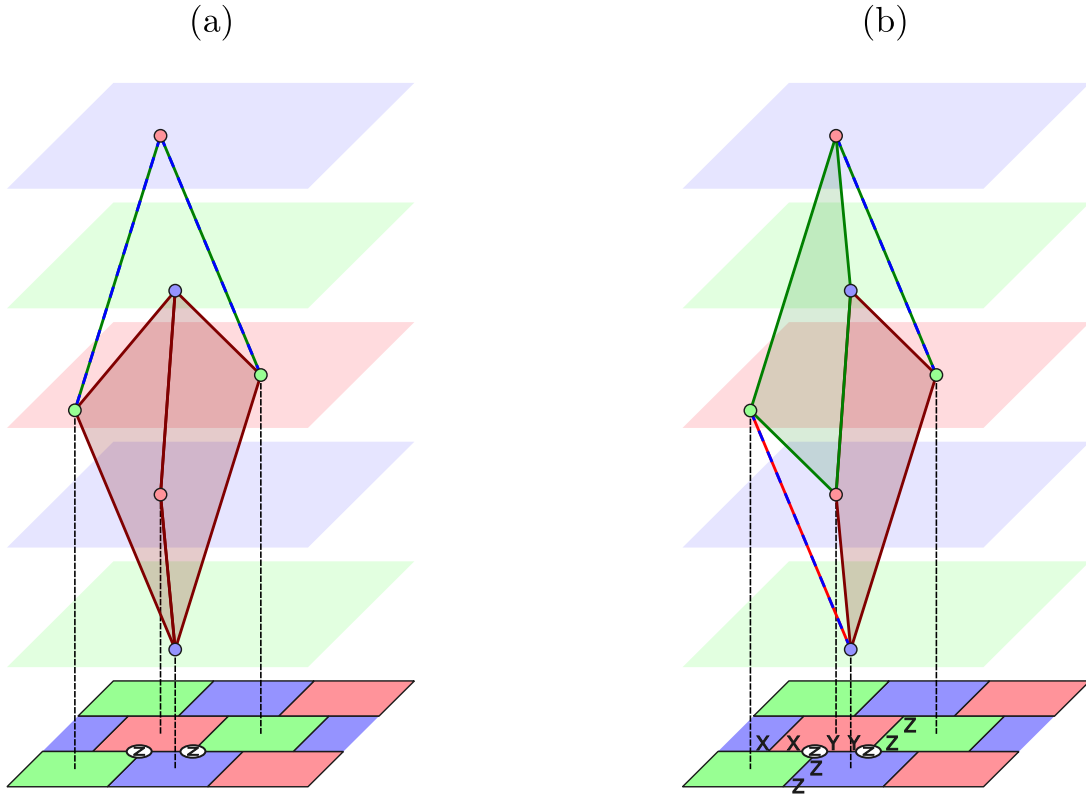


FIG. 15. Parts of the detector hypergraphs for the  $P^6$  (a) and the  $XYZ^2$  (b) honeycomb codes. Coloured layers indicate measurements performed in that time step. Coloured nodes are detectors. Hyperedges and edges are drawn between detectors corresponding to the syndromes of the single-qubit  $Z$  errors shown. The colour of the (hyper)edge denotes the time step during which the  $Z$  error generates the syndrome, e.g., a red hyperedge is the syndrome for a  $Z$  error occurring immediately after  $R$  check measurements. A blue/green dashed edge results from an error after blue or green check measurements.

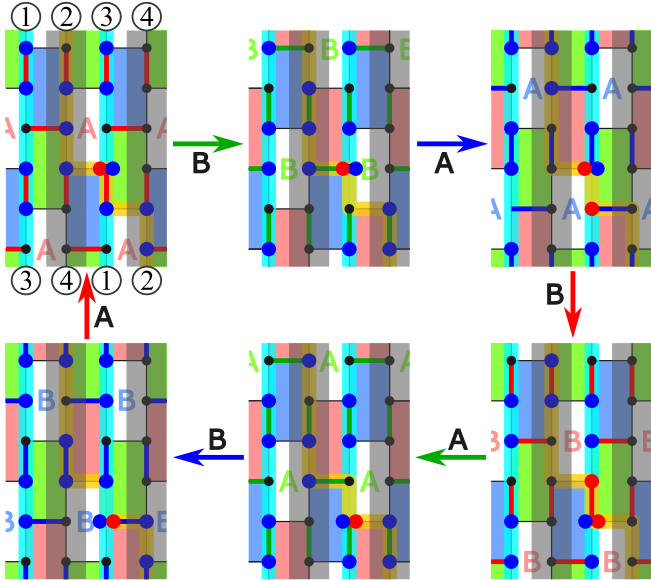


FIG. 16. Evolution of logical operators in the  $X^3Z^3$  Floquet code with a twisted boundary condition. Number-labelled edges (numbers are identified) at the top and bottom boundaries indicate the twisted boundary conditions. The logical operators are shown in light blue and yellow strips.

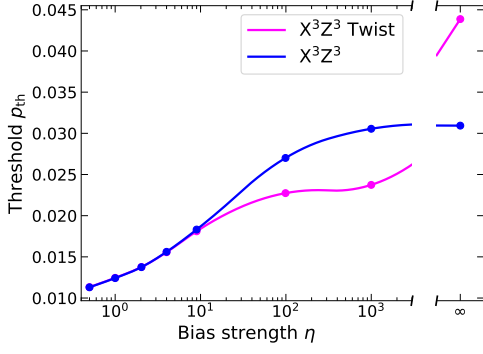


FIG. 17. Thresholds ( $p_{\text{th}}$ ) of  $X^3Z^3$  Floquet code with twisted (magenta) and untwisted (blue) periodic boundary condition as a function of noise bias  $\eta$ . We show some of the data points used in getting the thresholds in Fig. 18. Each of the data points is averaged over  $10^6$  Monte Carlo shots. For better visualisations, we fit all curves with quadratic splines.

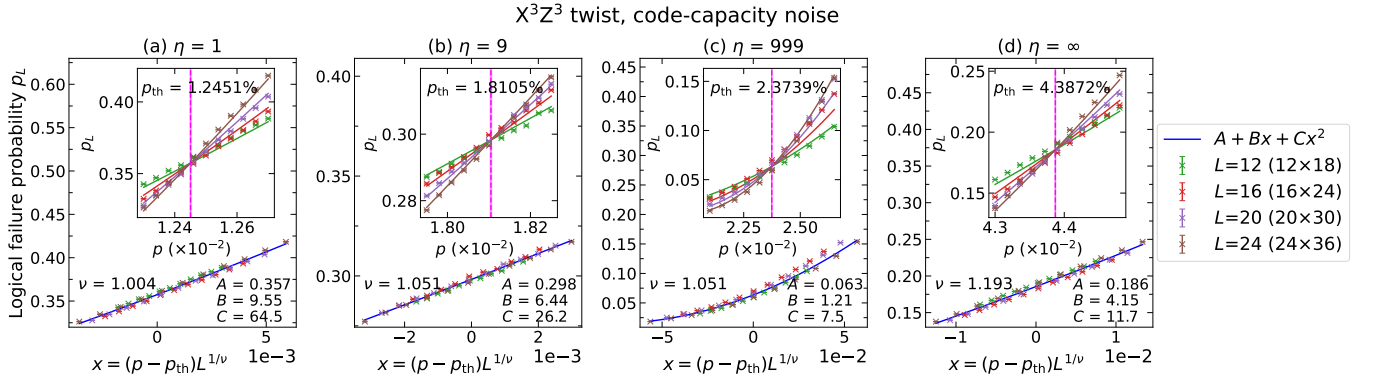


FIG. 18. Logical failure probability  $p_L$  of the  $X^3Z^3$  Floquet code with twisted periodic boundary condition as a function of  $x = (p - p_{\text{th}})L^{1/\nu}$ . The data shown are for different code sizes  $L \times 3L/2$  where  $L$  is the code length. The plots are calculated for the code capacity noise with various bias strengths: (a)  $\eta = 1$ , (b)  $\eta = 9$ , (c)  $\eta = 999$ , and (d)  $\eta = \infty$ . We fit the results to the function  $A + Bx + Cx^2$  (blue line). Insets: Logical failure probability  $p_L$  vs physical error rate  $p$ ; thresholds  $p_{\text{th}}$  are shown by the magenta vertical lines. Results for each code length  $L$  and physical error rate  $p$  are averaged over  $10^6$  number of shots.